# Critical Step in the HCl Oxidation Reaction over Single-Crystalline CeO$_{2-x}$(111):

## Peroxo-Induced Site Change of Strongly Adsorbed Surface Chlorine

Volkmar Koller,[1,2] Pablo Lustemberg,[1,3] Alexander Spriewald-Luciano,[1,2]

Sabrina M. Gericke,[4] Alfred Larsson,[5] Christian Sack,[1,2] Alexei Preobrajenski,[6]

Edvin Lundgren,[5] M. Veronica Ganduglia-Pirovano,[3]* Herbert Over[1,2]*

1) *Physical Chemistry Department, Justus-Liebig-University Giessen, Heinrich-Buff-Ring 17, 35392 Giessen, Germany*

2) *Center for Materials Research, Justus-Liebig-University Giessen, Heinrich-Buff-Ring 16, 35392 Giessen, Germany*

3) *Instituto de Catálisis y Petroleoquímica (ICP-CSIC), C/Marie Curie 2, 28049 Madrid, Spain*
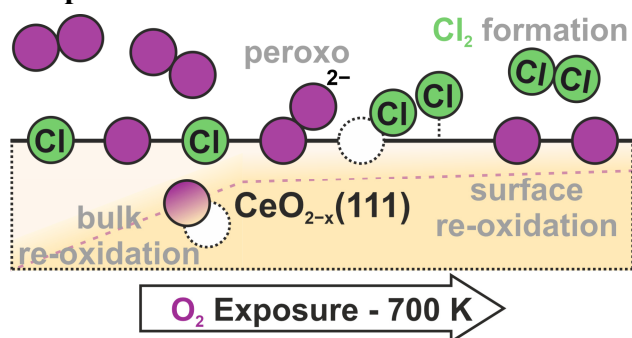
4) *Combustion Physics, Lund University, Box 118, 22100 Lund, Sweden*

5) *Synchrotron Radiation Research, Lund University, Box 118, 22100 Lund, Sweden*

6) *MAX IV Laboratory, Lund University, Box 118, 22100 Lund, Sweden*

*corresponding authors: E-mail: over@uni-giessen.de, vgp@icp.csic.es

**Graphical Abstract**



## Abstract

The catalytic oxidation of HCl by molecular oxygen (Deacon process) over ceria allows the recovery of molecular chlorine from omnipresent HCl waste produced in various industrial processes. Previous density functional theory (DFT) model-calculations[1] proposed, that the most critical reaction step in this process is the displacement of tightly bound chlorine at a vacant oxygen position on the CeO$_2$(111) surface (Cl$_{vac}$) towards a less strongly bound cerium on-top (Cl$_{top}$) position. This step is highly endothermic by more than 2 eV. On the basis of a dedicated model study, namely the re-oxidation of a chlorinated single crystalline Cl$_{vac}$-CeO$_{2-x}$(111)-($\sqrt{3} \times \sqrt{3}$)R30° surface structure, we provide unique spectroscopic data (high resolution core level spectroscopy (HRCLS) and X-ray adsorption near edge structure (XANES)) for this oxygen-induced de-chlorination process. Combined with theoretical evidence from DFT calculations, the Cl$_{vac} \rightarrow$ Cl$_{top}$ displacement reaction is predicted to be induced by a surface-adsorbed peroxo species (O$_2^{2-}$), making the displacement step concerted and exothermic by 0.6 eV with an activation barrier of only 1.04 eV. The peroxo species is shown to be important for the re-oxidation of Cl$_{vac}$-CeO$_{2-x}$(111) and is considered essential for understanding the function of ceria in oxidation catalysis.

**Keywords:** Deacon process, reduced ceria, peroxo surface species, displacement of strongly adsorbed chlorine, oxygen-induced de-chlorination process

## 1. Introduction

Hydrogen chloride (HCl) is a by-product in various industrial processes and accumulates to about 10 million tons annually that the market cannot adsorb.[2–4] A sustainable way to cope with this waste problem is to recover molecular chlorine from HCl by the heterogeneously catalyzed oxidation of HCl with molecular oxygen (Deacon process):

$$4\,HCl + O_2 \rightarrow 2\,Cl_2 + 2\,H_2O \qquad \Delta_r H = -114\ kJ/mol$$
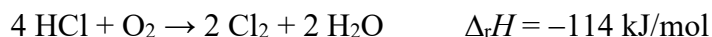
Although this process is known for more than 150 years,[5,6] only in the late 1990s a stable and active catalyst was discovered by Sumitomo Chemical based on $RuO_2$ covered on rutile $TiO_2$.[7] Some 15 years later, the HCl oxidation reaction over $CeO_2$-based catalysts[1,8,9] has been shown to be a promising and economically viable alternative to commercial $RuO_2$-based materials.

Based on experiments on ceria powder-catalysts, a reaction pathway for the HCl oxidation over the single crystalline $CeO_2(111)$ surface was proposed,[1,9] and the energies of the reaction intermediates were predicted using density functional theory (DFT) calculations (cf. **Figure 1**).
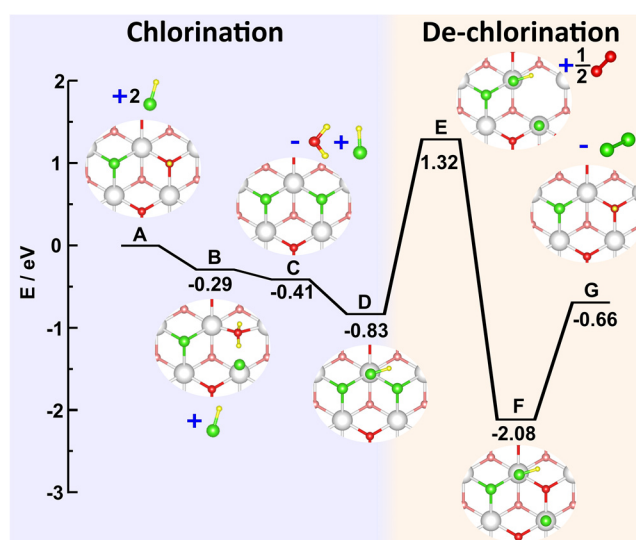


**Figure 1.** Proposed reaction pathway for the HCl oxidation over the single crystalline $CeO_2(111)$ surface (top view), re-arranged and based on Amrute et al.[1] Only the outermost O–Ce–O trilayer is depicted. Color code: $Ce^{4+}$ cations are white spheres, the O surface (subsurface) atoms are red (light red), Cl atoms are green and H atoms are yellow.

The catalytically active phase was identified with the chlorinated $CeO_2(111)$-$(2 \times 2)$ surface, where chlorine resides in an oxygen vacancy position and one surface lattice O site is occupied by hydrogen forming a hydroxyl group (**A**). The catalytic cycle[1] starts with the dissociative adsorption of HCl (acid-base reaction), where chlorine resides in a Ce on-top position ($Cl_{top}$) and the H atom is transferred to the OH surface group (**B**). The $Cl_{top}$ species displaces the formed $H_2O$ molecule and fills the nascent surface oxygen vacancy ($V_{O,S}$), thus becoming a second $Cl_{vac}$, while water desorbs at a typical reaction temperature of 700 K (**C**). A second HCl molecule dissociates on the surface and forms a $Cl_{top}$ species (**D**). The most critical but also innovative step in the proposed reaction pathway is the displacement of $Cl_{vac}$ to an on-top position $Cl_{top}$, a reaction step that is endothermic by 2.15 eV (**E**). The activation of $Cl_{vac}$ leaves an oxygen vacancy behind that is filled by dissociative adsorption of $1/2\ O_2$ from the gas phase, a process that is exothermic by 3.4 eV (**F**). Last, the two $Cl_{top}$ species recombine, leading to the desired $Cl_2$ product and closing the catalytic cycle (**G**). The latter steps of the reaction path in **Figure 1** can be considered an oxidative de-chlorination process (light orange background), while the first steps can be summarized as chlorination process of the surface (light blue background).

2

The proposed reaction pathway in **Figure 1** remains elusive in two critical points: First, the activation step $Cl_{vac} \rightarrow Cl_{top}$ is highly endothermic and therefore would only be realistic if it can be coupled with the exothermic adsorption process of 1/2 $O_2$ gas. The second point concerns the replenishment of a surface oxygen vacancy by 1/2 $O_2$ gas, which is not an elementary step. Instead, a full $O_2$ gas molecule has to be adsorbed, but where does then the other half of the $O_2$ molecule remain on the surface?

With these two questions in mind, we designed a dedicated surface science experiment, employing the recently developed $Cl_{vac}$-$CeO_{2-x}$(111)-$(\sqrt{3} \times \sqrt{3})$R30° model system.[10] The re-oxidation of $Cl_{vac}$-$CeO_{2-x}$(111)-$(\sqrt{3} \times \sqrt{3})$R30° is studied in situ by high-resolution synchrotron-based spectroscopy techniques, including high resolution core level shift spectroscopy (HRCLS) and X-ray absorption near edge spectroscopy (XANES), while the underlying re-oxidation steps are studied by density functional theory (DFT) calculations. Specifically, we elucidate the activation of displacing $Cl_{vac}$ towards $Cl_{top}$. This process is shown to be initiated by $O_2$ gas adsorption into an oxygen vacancy via the formation of a surface peroxide species (peroxo: $O_2^{2-}$), while its dissociation is coupled with the $Cl_{vac} \rightarrow Cl_{top}$ displacement. This renders the concerted $Cl_{vac}$ activation step slightly exothermic with an activation energy of only 1.04 eV.

## 2. Experimental and theoretical details

The lab-based experiments are performed in an ultrahigh vacuum (UHV) system that is equipped with Low-Energy Electron Diffraction (LEED) using a video-LEED (Specs ErLEED 1000-A) system. Additionally, Thermal Desorption Spectroscopy (TDS)/Temperature Programmed Desorption (TPD) is performed with a high sensitivity (ion counting) mass spectrometer (Hiden Analytical HAL 301/3F).[11,12] A second UHV system[13] is dedicated to lab-based XPS (Omnivac Al/Mg dual anode x-ray source and a Leybold EA 200 analyzer) that runs at a photon energy of 1253.6 eV (Mg). For the dosing of atomic oxygen O, the system is equipped with a thermal cracker (Oxford Applied Research: TC50 – Universal Thermal Cracker).

Basis of all experiments are single crystalline $CeO_2$(111) films on Ru(0001) (MaTeck GmbH, disk, ⌀ = 8 mm) prepared by physical vapor deposition (PVD) of Ce foil (HMW Hauner GmbH, 99.9%) from a well-outgassed electron beam evaporator (Focus GmbH, EFM 3, $U$ = 800 V, $P$ = 40−50 W, Flux = 2.0 µA, deposition time $t_{dep}$ = 70−120 min, Mo-crucible capacity = 250 mm³, contained Ce ≈ 25 mg). During evaporation, the sample is kept in a background $O_2$ atmosphere of $p(O_2)$ = 5·10⁻⁸ mbar at a temperature of $T$ = 700 K. Post-oxidation is achieved by annealing the sample to $T$ = 1000 K in $p(O_2)$ = 10⁻⁶ mbar for 15 min followed by flashing to $T$ = 1200 K and subsequent cooling to room temperature in $O_2$. The preparation process is adapted from that of Mullins et al.[14] and Hasegawa et al.[15] Similar preparation procedures were reported in the literature.[16−20] The film thickness of stoichiometric $CeO_2$(111) is determined by X-ray reflectometry (XRR, PANalytical X'Pert PRO MRD) to be 5.6 nm, corresponding to 18 O−Ce−O trilayers.[10]

The stoichiometric $CeO_2$(111)-Ru(0001) samples (prepared in the homelab at the JLU) are subsequently transferred to the preparation chamber of the permanent endstation EA01 (Surface and Material Science branch) at the FlexPES beamline[21] at MAX IV in Lund, Sweden. On-site the $CeO_2$(111)-Ru(0001) sample is annealed for $t$ = 15 min in $p(O_2)$ = 10⁻⁶ mbar followed by a quick annealing step to $T$ = 1200 K in $p(O_2)$ = 10⁻⁶ mbar to remove potential carbon contamination during the sample transfer. The reduced $CeO_{2-x}$(111) films are prepared by deposition of Ce metal under UHV conditions via PVD at room temperature on the preformed fully oxidized $CeO_2$(111) layer that is followed by an annealing step of the sample to $T$ = 900 K for 15 min and a final annealing step $T$ = 1100 K under UHV conditions.[19,22,23] We employed

the same electron beam evaporator as used at the JLU for depositing metallic Ce under UHV conditions for a deposition time of $t_{reox} \approx 0.12\ t_{dep}$. After the beamtime XRR was employed to determine the thickness of the prepared $CeO_{2-x}(111)$ film on Ru(0001) to be 7.5 nm that corresponds to 24 O−Ce−O trilayers (cf. **Figure S1**). The fully chlorinated $CeO_{2-x}(111)$ film is prepared by exposing the $CeO_{2-x}(111)$ film to 15 L HCl (ultrapure HCl, Air Liquide, 2.8) at room temperature and subsequent flashing to $T = 1000$ K, revealing a $(\sqrt{3} \times \sqrt{3})$R30° LEED pattern (cf. **Figure S2**). The annealing step leads to the removal of hydrogen from the surface via water or $H_2$ formation. Recently, it was demonstrated[10] that adsorbed chorine on $CeO_{2-x}(111)$ only resides exclusively in surface oxygen vacancies ($Cl_{vac}$): $Cl_{vac}$-$CeO_{2-x}(111)$-$(\sqrt{3} \times \sqrt{3})$R30°.

The measurement protocol in the re-oxidation experiments of fully chlorinated $Cl_{vac}$-$CeO_{2-x}(111)$ is adjusted to the requirements of the FlexPES beamline at MAX IV in Lund, Sweden in that the $O_2$ pressure in the analysis chamber must not raise above $10^{-8}$ mbar. This excludes an operando experiment so that we exposed $O_2$ to the $Cl_{vac}$-$CeO_{2-x}(111)$ at a sample temperature of 700 K in the preparation chamber first and then transferred the sample back to the analysis chamber without breaking the UHV conditions, where high resolution core level shift spectroscopy (HRCLS) and X-ray absorption (XANES) data are acquired.

HRCLS of Ce 4d, Cl 2p, and O 1s at two photon energies (Ce 4d: $hv = 250$ eV/850 eV; Cl 2p: $hv = 250$ eV/850 eV; O 1s: $hv = 580$ eV/1180 eV) allows us to probe both near-surface and bulk-like properties. Bulk-like properties are probed by photoelectrons with kinetic energy of $E_{kin} = 650$ eV, while near-surface properties are probed by photoelectron of $E_{kin} = 50-130$ eV kinetic energy, close to the minimum of the universal curve of inelastic mean free path of electrons.[24] The energy of the Ce 4d was chosen to be $hv = 250$ eV as a compromise between achieving high surface sensitivity and avoiding the cooper minimum[25] at $hv = 175$ eV[26] with its low cross section. HRCLS of Ce 4d is used instead of Ce 3d to have sufficient flux at higher kinetic energies of $E_{kin} = 650$ eV. The slit-width of the beam is set to 50 µm and the pass energy $E_{pass}$ of the detector is set to $E_{pass} = 50$ eV, except for Cl 2p ($hv = 250$ eV, $E_{pass} = 10$ eV) and O 1s ($hv = 580$ eV, $E_{pass} = 20$ eV). The spectra are calibrated via the Fermi level $E_F$ of gold foil mounted next to the sample. From the Ce 4d spectra at $hv = 250$ eV the near-surface fraction of $Ce^{3+}/Ce^{4+}$ and therefore the near-surface reduction degree $x$ ($Ce^{3+}$ fraction) can be determined. XANES data of Ce $M_{4,5}$ edge (Ce 3d) in total electron yield (TEY) mode provides true bulk information of the $Ce^{3+}/Ce^{4+}$ fraction and therefore on the bulk reduction degree $x$ ($Ce^{3+}$ fraction). Beam-induced damages of the studied layers are not encountered, as routinely checked during the synchrotron beamtime. Additionally, the defocused spot is moved between each measuring point over the homogeneous sample. Altogether, this powerful combination of synchrotron-based techniques allows us disentangling surface from bulk properties and is applied here to study the re-oxidation and de-chlorination of $Cl_{vac}$-$CeO_{2-x}(111)$.

We perform spin-polarized DFT calculations utilizing the slab−supercell technique.[27] The Vienna Ab-initio Simulation Program (VASP, version 5.3.5 and 5.4.4)[28−32] is employed for this purpose. In our calculations, the Ce (4f, 5s, 5p, 5d, 6s), O (2s, 2p), Cl (2s, 2p), and H (1s) electrons are explicitly treated as valence states using the projector augmented wave (PAW) method.[33] A plane-wave cutoff energy of 400 eV is applied, while the remaining electrons are considered part of the atomic cores. For the determination of energies and forces, we adopt the DFT+U approach proposed by Dudarev et al.[34] with a $U_{eff}$ value of U − J = 4.5 eV for the Ce 4f electrons. Additionally, we employ the generalized gradient approximation (GGA) as suggested by Perdew, Burke, and Ernzerhof (PBE).[35]

The $CeO_{2-x}(111)$ surfaces are modeled with an optimized lattice constant of 5.485 Å for bulk $CeO_2$. The Cl surface phase is modeled based on (3 × 3) unit cell reported by Olbrich et al.[36]

4

for describing the formation of reduced $CeO_{2−x}(111)$ surface reconstructions with one surface ($V_{O,s}$) and two subsurface ($V_{O,ss}$) vacancies in the outermost O−Ce−O trilayer. All surface models used in this work have three O−Ce−O trilayers and ~21 Å of vacuum separation between consecutive slabs. A $(2 × 2 × 1)$ $k$-point mesh according to the Monkhorst−Pack method is used to sample the Brillouin zone.[37] For the gas-phase calculations of the HCl, $O_2$ and $Cl_2$ molecules, a cell of $(15 × 15 × 15)$ Å$^3$ is employed, using only the Γ-point.

The average adsorption energy per Cl atom on the $CeO_{2−x}(111)$ surface is calculated according to the following equation: $E_{ads} = (E[nCl/CeO_{2−x}(111)] − E[CeO_{2−x}(111)] − n/2\ E[Cl_2 gas])/n$, where $n = 1,2,3$ is the number of adsorbed Cl atoms, $E[nCl/CeO_{2−x}(111)]$ is the total energy of the Cl atoms adsorbed on the surface, $E[CeO_{2−x}(111)]$ is the total energy of the surface without the adsorbate, and $E[Cl_2 gas]$ is the energy of the chlorine molecule in gas phase.

To locate transition state (TS) structures, we employ the climbing image nudged elastic band method (CI-NEB)[38] with seven images for each reaction pathway. For all the TS reported in this work, we have found only one imaginary frequency, and the full geometry optimizations starting from its back and forward nearest configurations (along the reaction path) end in a non-dissociated and dissociated state, respectively. In the calculated potential energy profiles, the energy barrier, $E_{Barrier} = E_{TS} − E_{IS}$, equals the difference between the energy of the transition state, $E_{TS}$, and the initial state, $E_{IS}$, whereas the effective or apparent energy barrier is given by the energy of the transition state, $E_{TS}$, referenced to $n/2$ $Cl_2$ gas and the clean surface.

## 3. Results

### 3.1 Synchrotron-based characterization of $Cl_{vac}$-$CeO_{2−x}(111)$-$(\sqrt{3} × \sqrt{3})R30°$

The on-site prepared $Cl_{vac}$-$CeO_{2−x}(111)$-$(\sqrt{3} × \sqrt{3})R30°$ is thoroughly characterized by HRCLS and XANES measurements. The (bulk) reduction degree $x$ and corresponding $Ce^{3+}$ fraction $(2x·100\%)$ of $CeO_{2−x}(111)$ is derived from the Ce $M_{4,5}$ edge XANES spectrum (TEY yield) by fitting the XANES spectrum of $CeO_{2−x}(111)$ as a linear combination of the reference spectra of the fully oxidized $CeO_2(111)$ film (0% $Ce^{3+}$) and a fully reduced $Ce_2O_3$ film (100% $Ce^{3+}$): $(1−2x)·XANES(CeO_2) + 2x·XANES(Ce_2O_3)$. The fully reduced $Ce_2O_3$ films is prepared in-situ by depositing ($U = 800$ V, $P = 40$-$50$ W, Flux = 2.0 µA, deposition time $t_{dep} = 30$ min) metallic Ce on Ir(111) under UHV conditions and annealing the film to 1250 K. The residual water pressure in the UHV chamber is sufficient to oxidize the Ce film to $Ce_2O_3$. The corresponding spectra of $Ce_2O_3$ (HRCLS-Ce 4d, XANES Ce $M_{4,5}$ edge) agree well with those reported in the literature.[39−43]

All XANES spectra including the reference spectra are normalized by the energy dependent flux and the integral intensity in the range from 865.5 eV to 918.5 eV (**Figure S3**). The procedure of linear combination is summarized in **Figure S3b**, resulting in a bulk $Ce^{3+}$ fraction of 37% that is in between those of $(3 × 3)$ and $(\sqrt{7} × \sqrt{7})R19.1°$. Accordingly, in LEED a faint $(3 × 3)$ is visible (cf. **Figure S2a**). Upon 15 L HCl exposure and subsequent stepwise annealing a $(\sqrt{3} × \sqrt{3})R30°$ overlayer of chlorine is formed (cf. **Figure S2b**). Recall that the very same $(\sqrt{3} × \sqrt{3})R30°$ chlorine overlayer structure is observed for a variety of reduction degrees $CeO_{2−x}(111)$ ranging from a $Ce^{3+}$ fraction of ~40% to ~80%.[10]

Ce 4d HRCL spectra of $CeO_{2−x}(111)$ and $Cl_{vac}$-$CeO_{2−x}(111)$ including the reference spectra of $Ce^{4+}$ and $Ce^{3+}$ are summarized in **Figure S4.** Again, by employing the linear combination of $CeO_2(111)$ and $Ce_2O_3$ Ce 4d reference (HRCL) spectra, the $Ce^{3+}$ fraction in the near-surface region can be determined (cf. **Figure S4b**). The near surface $Ce^{3+}$ fraction of 71% is significantly higher than in the bulk, fully consistent with recent studies from the Matolin´s group.[22]

5

The Cl 2p HRCL spectra after 15 L HCl exposure to $CeO_{2-x}(111)$ and subsequent annealing to 1000 K are presented in **Figure S5**. The shoulders at lower binding energy of the Cl 2p doublet at 198.6 eV/200.2 eV are assigned to chlorine still forming a hydrogen bond.[44] These shoulders disappear upon annealing to 1000 K, leaving only a single Cl component on the surface. Concomitant with the decline of the shoulder in Cl 2p, also the OH species[45] in the O 1s spectrum (cf. **Figure S6**) disappear. The O 1s spectrum of fully chlorinated $Cl_{vac}$-$CeO_{2-x}(111)$ is shifted by 0.39 eV when compared to that of the stoichiometric $CeO_2(111)$ (cf. **Figure S7**).

**3.2 Re-oxidation and De-chlorination experiments of $Cl_{vac}$-$CeO_{2-x}(111)$**

The re-oxidation experiments of the chlorinated $CeO_{2-x}(111)$ is carried out stepwise by a specific exposure of $O_2$ at 700 K followed by a subsequently characterization of the sample with XANES and HRCLS at room temperature. The temperature of 700 K is chosen to be identical with the typical reaction temperature of the ceria-based Deacon process. We start the discussion with XANES Ce $M_{4,5}$ edge (Ce 3d) data in the total electron yield (TEY) mode (cf. **Figure 2**). This detection mode is truly bulk sensitive to Ce, so that the $Ce^{3+}$ fraction of the entire $Cl_{vac}$-$CeO_{2-x}(111)$ film can be quantified by a linear combination of the reference spectra, as discussed in **section 3.1**.
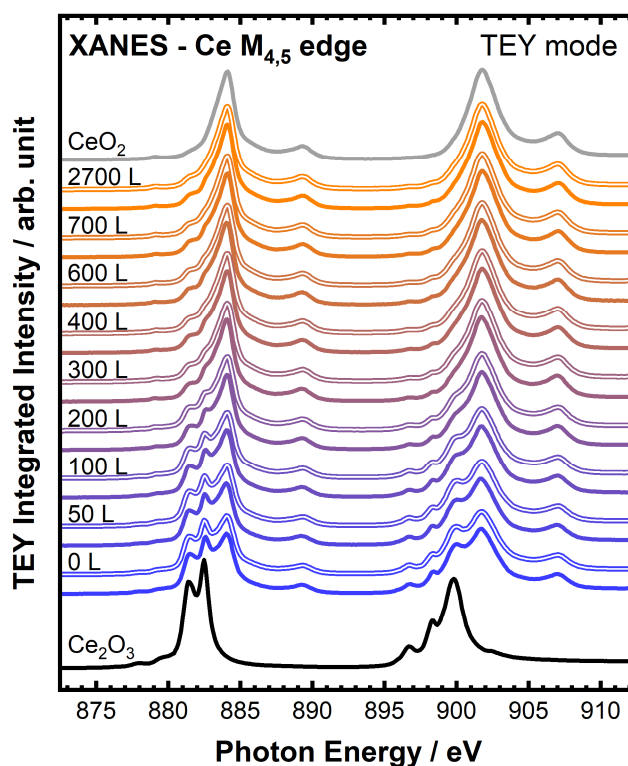


**Figure 2.** Bulk re-oxidation of $Cl_{vac}$-$CeO_{2-x}(111)$: Bulk sensitive XANES Ce $M_{4,5}$ edge (Ce 3d) data (total electron yield: TEY) after exposing of $Cl_{vac}$-$CeO_{2-x}(111)$ to various doses of $O_2$ at 700 K indicated in Langmuir (L). The reference spectra for fully oxidized $CeO_2$ and fully reduced $Ce_2O_3$ are superimposed and serve as references for fitting by a linear combination of these reference spectra to determine the bulk $Ce^{3+}$ fraction. The optimized linear combination for each spectrum are shown as thin double line (shifted for clarity reasons) in the same color as the experimental spectra.

The high quality of these fits can be judged from inspection of **Figure 2**, while the derived bulk $Ce^{3+}$ fraction as a function of $O_2$ exposure is compiled in **Figure 3** (circles). Clearly, the bulk $Ce^{3+}$ fraction decreases linearly with $O_2$ exposure: first steeply from 38% to 11% upon 300 L of $O_2$ and then slows down from 11% to 7% when increasing the $O_2$ exposure from 300 L to 700 L (and 5% for 2700 L $O_2$).
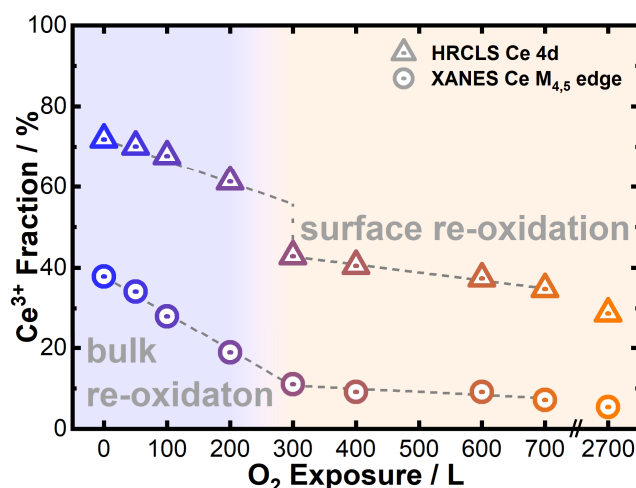
6

**Figure 3.** Bulk and surface re-oxidation of $Cl_{vac}$-$CeO_{2-x}(111)$: The bulk $Ce^{3+}$ fraction (XANES, circles) of Cl-$CeO_{2-x}(111)$ depending on the $O_2$ exposure compared to the near-surface $Ce^{3+}$ fraction as derived from HRCL Ce 4d spectra ($hv = 250$ eV, triangles).

While XANES in the TEY mode is bulk-sensitive, photoemission data of Ce 4d employing a photon energy of $hv = 250$ eV photoelectrons with a kinetic energy of $E_{kin} \approx 120$ eV are highly surface sensitive (the escape depth of photoelectrons is about 1nm).[24] Also the Ce 4d spectra in **Figure 4** can be fitted by a linear combination of references Ce 4d spectra of $Ce_2O_3$ and $CeO_2$. Even without fitting it is obvious (consider the two peaks W''' and X''', assigned to a Ce $4d^9$ O $2p^6$ Ce $4f^0$ final state of $Ce^{4+}$ at $E_{BE} \approx 122–126$ eV)[41,46] that the Ce 4d spectra decompose in two sets. At low $O_2$ exposures up to 200 L, the Ce 4d spectra vary slightly with exposure from 72% to 61% $Ce^{3+}$. Between 200 L and 300 L of $O_2$ an abrupt change in the Ce 4d spectra occurs reducing the $Ce^{3+}$ fraction from 61% to 43%. For higher $O_2$ exposures above 300 L the variation in Ce 4d spectra is small again (43% to 35% $Ce^{3+}$). In fact, this observation is fully reconciled and quantified with the fitting procedure (**Figure 4**) whose derived near-surface $Ce^{3+}$ fractions are overlaid in **Figure 3** (triangles). For $O_2$ exposure below 200 L (**Figure 3**, blue background), the fraction of near surface $Ce^{3+}$ of $CeO_{2-x}(111)$ decreases more slowly than that of bulk $Ce^{3+}$ as derived from the XANES data.

Keeping in mind that XANES in TEY mode is bulk-sensitive, while Ce 4d spectra is essentially surface sensitive, the difference in $Ce^{3+}$ fraction (bulk versus surface) as a function of $O_2$ exposure is explained by a preferential oxidation of bulk $CeO_{2-x}(111)$. In the $O_2$ exposure ranging from 200 L to 300 L, the near surface $Ce^{3+}$ fraction decreases quickly, while the bulk $Ce^{3+}$ fraction (XANES) of the entire film still decreases with the same rate as for lower exposures (**Figure 3**, transition blue/orange). This behavior points to a preferential oxidation of the surface region for $O_2$ exposures 200 L–300 L. Above 300 L both bulk and surface region further oxidize slowly with the $Ce^{3+}$ fraction declining faster in the surface than in the bulk region (**Figure 3**, blue background). Even after exposure of 2700 L of $O_2$ the $Ce^{3+}$ fraction in the near surface region is still 30%, while that of the bulk $Ce^{3+}$ is 5%. The mechanisms for the initial bulk oxidation followed by the surface oxidation will be further discussed in **section 3.3**.

It is known that the O 1s binding energy depends sensitively on the reduction degree $x$ of $CeO_{2-x}$.[19,47] In **Figure S7a** we show surface-sensitive O 1s spectra ($hv = 580$ eV) depending on the applied $O_2$ exposure during re-oxidation. Up to 200 L $O_2$, a shift by 0.1 eV is observed in the O 1s binding energy, while from 200 L to 300 L, it additionally shifts by 0.1 eV, remaining then nearly constant for even higher $O_2$ exposures. The final O 1s is shifted to lower binding energy when compared with the stoichiometric $CeO_2(111)$ surface (cf. **Figure S7a**). For resolving this small energy shift, high resolution at FLEXPES is mandatory. More bulk-

sensitive O 1s spectra are shown in **Figure S7b**. Here a more continuous shift of the O 1s binding energy is evident, consistent with the XANES experiments shown in **Figure 2**.
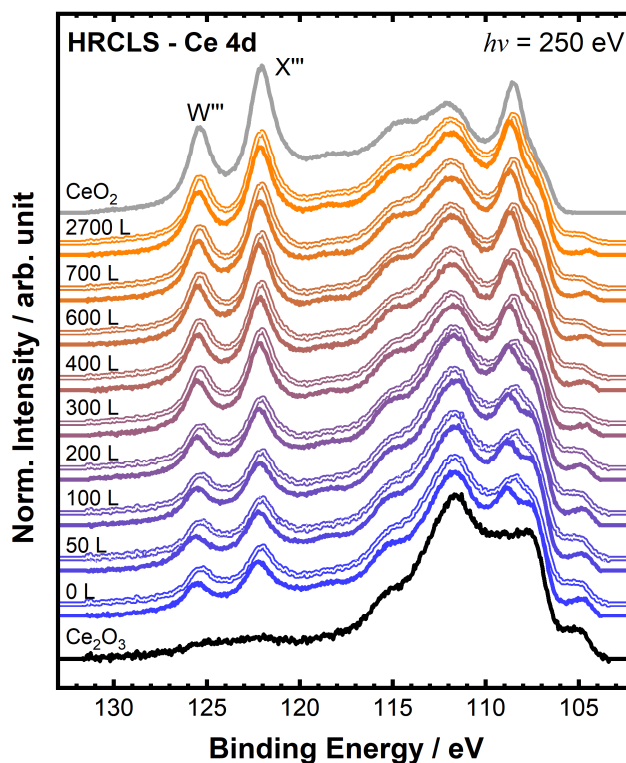


**Figure 4.** Surface re-oxidation of $Cl_{vac}$-$CeO_{2-x}$(111): Surface sensitive Ce 4d spectra ($hv = 250$ eV) after exposing of Cl-$CeO_{2-x}$(111) to various doses of $O_2$ at 700 K indicated in Langmuir (L). The reference spectra for fully oxidized $CeO_2$ and fully reduced $Ce_2O_3$ are superimposed and serve as references for fitting by a linear combination of these reference spectra to determine the near-surface $Ce^{3+}$ fraction. The optimized linear combination for each spectrum are overlaid as thin double line (shifted for clarity reasons) in the same color as the experimental spectra.

In **Figure 5** we summarize the surface sensitive Cl 2p photoemission data ($hv = 250$ eV) of Cl-$CeO_{2-x}$(111) exposed to various doses of $O_2$ at 700 K. Up to 200 L of $O_2$ no significant changes are discernible in the Cl 2p spectra (Cl $2p_{1/2}$ and Cl $2p_{3/2}$ at 200.9 eV and 199.3 eV). That is, the changes are minor as long as the $Ce^{3+}$ fraction in the surface near region does not change significantly (cf. **Figure 3**). For higher $O_2$ exposures the Cl 2p duplet shifts then to lower binding energies by 0.3 eV (majority species) and by 1.0 eV (minority species: shoulder at 198.3 eV, cf. **Figure S9**).

This abrupt change in the Cl 2p spectra at 300 L coincides with the sudden decrease in the surface $Ce^{3+}$ fraction as indicated in **Figures 3**. For a site change the shift in Cl 2p is likely to be too small, when compared to chlorine adsorption on $RuO_2$(110), where a site change of Cl from on-top to bridge position leads to a Cl 2p binding energy shift of 1.5 eV.[48,49] A change in the oxidation state of $Cl_{vac}$ from −1 to 0 can clearly be excluded since $Cl^-$ is substantially stronger bound (DFT: 2.65 eV) than $Cl^0$ (DFT: 0.46 eV) in a vacancy position (cf. **Figure S8**).

Therefore, the small energy shift of 0.3 eV (main peak) and 1.0 eV for the shoulder in Cl 2p with respect to the 0L spectrum may be traced to the existence of two different chlorine $Cl_{vac}$ species as a consequence of the re-oxidation of the surface. In **Figure S9** we exemplify the deconvolution of the surface sensitive Cl 2p spectra of $Cl_{vac}$-$CeO_{2-x}$(111) in comparison with that after exposing 2700 L of $O_2$ at 700 K. Similar Cl 2p spectra are recorded with $hv = 850$ eV (**Figure S10**; more bulk-sensitive), evidencing that both chlorine species are located solely at the surface and the quantification of chlorine species is not affected by diffraction effects. When

increasing the surface temperature from 700 K to 800 K, 900 K, 1050 K, and finally to 1200 K, the Cl 2p spectra in **Figure S11** indicate that both Cl species are stable up to 900 K and the minority Cl component desorbs at slightly lower temperatures than the chlorine in the main peak. This indicates a lower thermal stability of the minority species than that of the majority chlorine species.
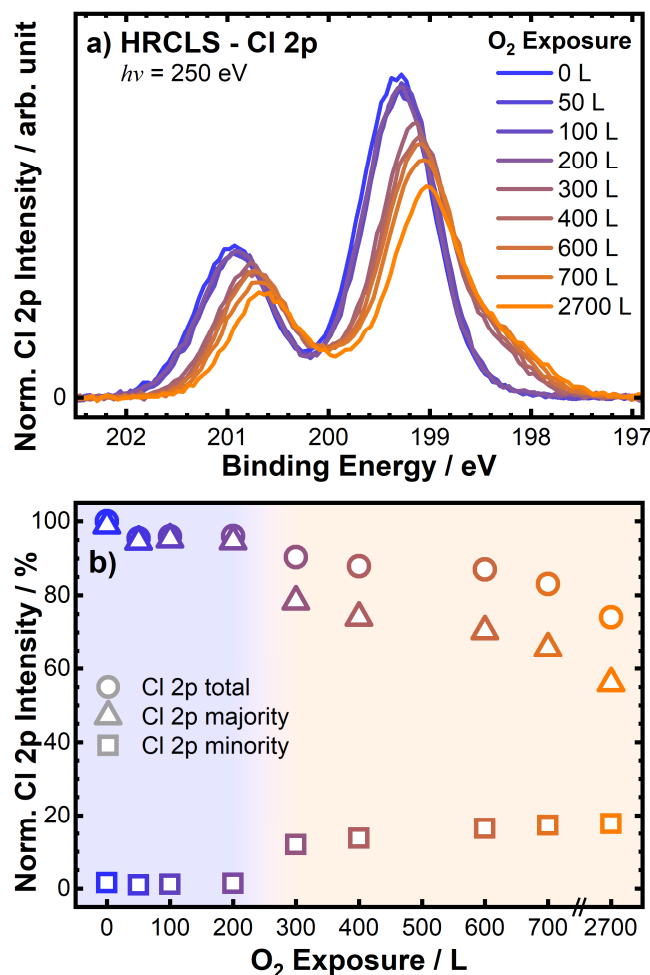


**Figure 5.** De-chlorination experiment: a) Cl 2p core level spectra ($h\nu = 250$ eV) after exposing of $Cl_{vac}$-$CeO_{2-x}(111)$ to various doses of $O_2$ at 700 K indicated in Langmuir (L). b) Intensity Cl 2p core level spectra after exposing of $Cl_{vac}$-$CeO_{2-x}(111)$ to various doses of $O_2$ at 700 K indicated in Langmuir (L).

The evaluation of the total amount of Cl (cf. **Figure 5b**) as a function of $O_2$ exposure at 700 K indicates a ~25% loss of surface chlorine above an exposure of 300 L $O_2$. Oxygen induced removal of chlorine is only observed for the majority Cl 2p component, while the minority Cl species is not affected by $O_2$ exposure at 700 K and is therefore not relevant for the present de-chlorination step. This indicates a higher chemical stability of the minority species with respect to $O_2$ exposure at 700K.

The loss of 25% Cl may be traced to a destabilization of the chlorine species due to re-oxidation. In a recent study,[10] the Cl-overlayer on $CeO_{2-x}(111)$ was shown to destabilize with decreasing $Ce^{3+}$ fraction of the underlying preformed $CeO_{2-x}(111)$ thin film of ~40% to ~80% ($0.2 < x < 0.4$). Therefore, we compare in **Figure 6** lab-based $Cl_2$ thermal desorption spectra of $Cl_{vac}$-$CeO_{2-x}(111)$ with ~37% $Ce^{3+}$ fraction (identically prepared as at the beamtime) before and after re-oxidation, clearly indicating that re-oxidation of the chlorinated $CeO_{2-x}(111)$ substantially shifts the desorption temperature of chlorine to lower temperatures, i.e., the adsorbed chlorine is significantly destabilized by the re-oxidation process. However, these

experiments also show that the loss of 25% of Cl cannot be explained by this destabilization effect, since the desorption onset occurs at a temperature of 800 K (cf. **Figure 6**) which is significantly higher than 700 K. Therefore, the $O_2$ induced removal of $Cl_{vac}$ needs to be a surface reaction rather than a simple desorption process.

The broad TD feature of $Cl_2$ in TDS (**Figure 6**) of re-oxidized $Cl_{vac}$-$CeO_{2-x}$(111) from 800 K to 1200 K may be traced to a varying $Ce^{3+}$ fraction near the surface. During $Cl_2$ desorption two oxygen vacancies per $Cl_2$ are left on the surface so that the near-surface $Ce^{3+}$ fraction increases, which leads to stronger Cl bonding leading to the broad feature in $Cl_2$-TDS (cf. **Figure 6**) consistent with previous DFT calculations.[10]
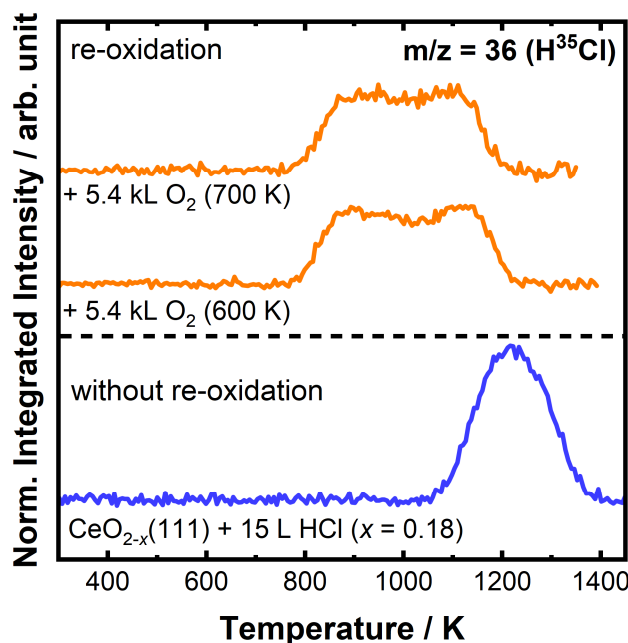


**Figure 6.** HCl thermal desorption spectra of a saturated Cl overlayer on $CeO_{2-x}$(111) surfaces before and after re-oxidation (2700 L $O_2$) at 700 K and 600 K.

### 3.3 Re-oxidation and De-chlorination of $Cl_{vac}$-$CeO_{2-x}$(111): Theory

In the following we study three major steps in the re-oxidation and de-chlorination of $Cl_{vac}$-$CeO_{2-x}$(111), namely $O_2$ activation, re-oxidation of $CeO_{2-x}$(111), and finally the partial de-chlorination of $Cl_{vac}$-$CeO_{2-x}$(111). These processes are modeled by a $Ce_3O_5$(111)-(3 × 3) unit cell[50] with a $Cl_{vac}$ coverage of 1/3 and with or without O vacancies in deeper oxygen layers below the surface ($V_{O,SSS}$).

Let us start with the $O_2$ activation. For $O_2$ adsorption to occur we need the presence of a surface oxygen vacancy ($V_{O,S}$). $O_2$ species adsorbing on surface Ce sites are weakly bound by less than 0.4 eV,[51,52] thus being irrelevant for the re-oxidation process studied at 700 K. The formation of a surface O-vacancy at the $3Cl_{vac}$-$Ce_3O_5$(111)-(3 × 3) surface by desorption of molecular oxygen (1/2 $O_2$) requires 2.18 eV (**Figure S12a-b**, no $V_{O,SSS}$ in the slab) and can therefore be safely ruled out at 700 K. Instead, the diffusion of an O vacancy from a deeper oxygen layer ($V_{O,SSS}$) of $Ce_3O_5$(111) towards the surface is preferred as summarized in the energy diagram, presented in **Figures 7a** and **S12d** (one $V_{O,SSS}$ in the slab). The O vacancy can easily diffuse towards the surface with an activation energy of 0.80 eV. The subsurface oxygen vacancy ($V_{O,SS}$) is the most preferred site. The surface O vacancy ($V_{O,S}$) is 0.16 eV less preferred than subsurface vacancy ($V_{O,SS}$) and the activation barrier for an oxygen vacancy to diffuse from the subsurface to the surface is 0.52 eV.[53-55] The probability for an oxygen vacancy to be encountered at the surface is given by Boltzmann statistics. For instance, at 700 K, the probability of a surface oxygen vacancy ($V_{O,S}$) is about 7%. Whenever an $O_2$ molecule from

the gas phase strikes a surface oxygen vacancy ($V_{O,S}$), $O_2$ is strongly adsorbed by about 2 eV in the form of a peroxo-species ($O_2^{2-}$) and pins the vacancy to the surface. The O–O bond length is 144 pm that agrees well with a typical bond length of peroxide groups.[56] The oxidation state of $O_2$ is determined by counting the number of $Ce^{3+}$ sites left in the unit cell. Upon $O_2$ adsorption this number is reduced by two per (3 × 3) cell, clearly evidencing[57] that the adsorbed $O_2$ is in the oxidation state 2−, i.e., forming a peroxo species $O_2^{2-}$. The peroxo species cannot further dissociate to $O_{top}$ and $O_{vac}$ species, since this process is endothermic by about 0.48 eV (**Figure 7b**).
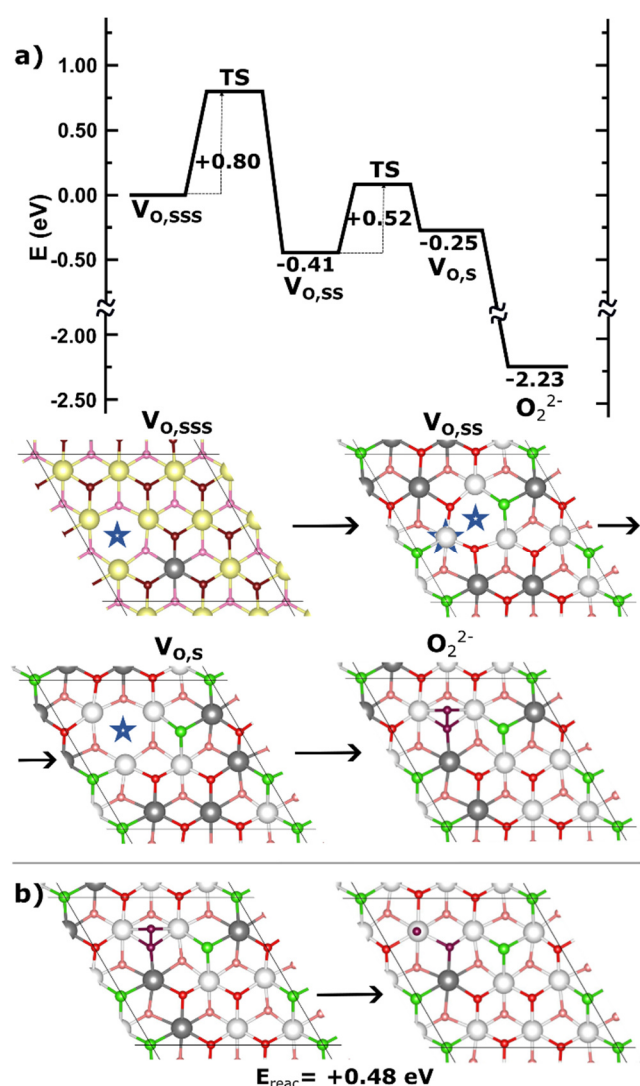


**Figure 7.** $O_2$-activation at $3Cl_{vac}$- $Ce_3O_5(111)$-(3 × 3): a) Energy diffusion path of the oxygen vacancy from the third oxygen layer ($V_{O,SSS}$) to the surface ($V_{O,S}$) of $3Cl_{vac}$-$Ce_3O_5(111)$ and the $O_2^{2-}$ adsorption state on the oxygen vacancy (peroxo species: $O_2^{2-}$). b) Adsorption and c) Dissociation of adsorbed peroxo to $O_{top}$ and $O_{vac}$ species. Color code: $Ce^{4+}$ on the first/second ceria trilayer are white/yellow and $Ce^{3+}$ atoms are gray, the oxygen surface (subsurface) atoms are red (light red), and Cl atoms are in green. The blue star indicates the oxygen vacancy.

The energy profile for the re-oxidation of $Cl_{vac}$-$CeO_{2-x}(111)$ (cf. **Figure 8**) starts from the adsorbed surface peroxo species and assumes the existence of oxygen vacancies in deeper ceria layers ($V_{O,SSS}$ in the slab). If one of these vacancies diffuses towards the surface and the subsurface vacancy ($V_{O,SS}$) is near the peroxo species, dissociation of the peroxo species occurs. This dissociation step is exothermic by 2.41−2.58 eV and is only slightly activated by 0.31−0.68 eV depending on the local configuration. Two lattice oxygen atoms are formed, thereby annihilating two oxygen vacancies, one on the surface ($V_{O,S}$) and the other in the

subsurface ($V_{O,SS}$) underneath. This process reduces the concentration of oxygen vacancies in the near-surface region so that the chemical potential difference drives the diffusion from bulk vacancies to the surface (activation barrier: 0.80 eV), thereby re-oxidizing the bulk of $CeO_{2-x}(111)$.
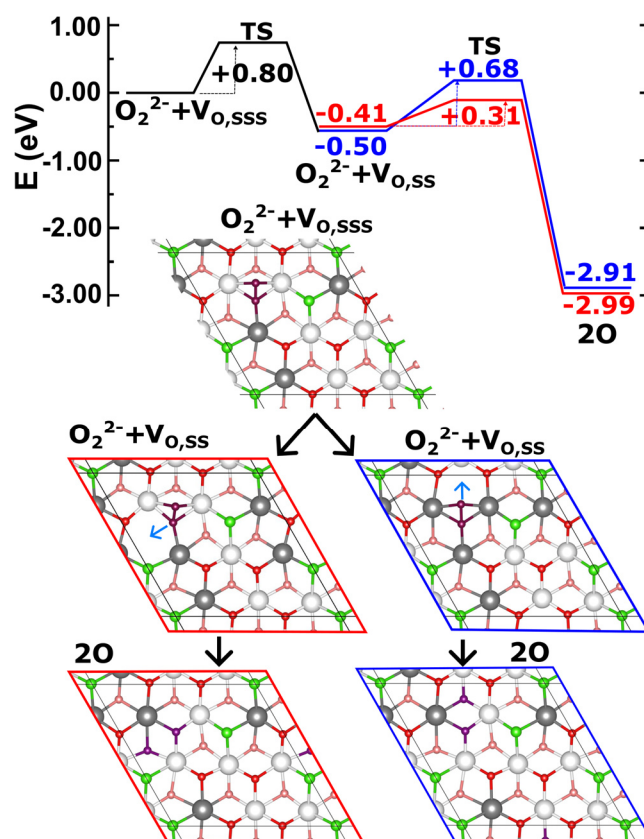


**Figure 8.** Re-oxidation process of $3Cl_{vac}$-$Ce_3O_5(111)$-$(3 \times 3)$. The first step is the diffusion of an oxygen vacancy $V_{O,sss}$ to $V_{O,ss}$. Then $O_2^{2-}$ dissociates and fills in the $V_{O,ss}$. Depending on the local configuration this dissociation process is activated by 0.31 eV or 0.68 eV. Color code: $Ce^{4+}$ are white and $Ce^{3+}$ atoms are gray, the oxygen surface (subsurface) atoms are red (light red), and Cl atoms are in green. The adsorbed $O_2^{2-}$ is depicted in violet, the blue arrow indicates the movement of the O atom that fills the $V_{O,S}$ upon $O_2^{2-}$ dissociation.

We consider now the displacement step of $Cl_{vac}$ to $Cl_{top}$, a process that is shown to be induced by the peroxo species at the surface and whose energy profile is depicted in **Figure 9**, calculated using a structure with two $O_2^{2-}$ species (no $V_{O,SSS}$ in the slab). As soon as the peroxo species is in the proximity of a $Cl_{vac}$ species, the dissociation of the $O_2^{2-}$ species leads to the displacement of $Cl_{vac}$ to $Cl_{top}$ which is exothermic by 0.60 eV with an activation barrier of 1.04 eV. This concerted process is shown as movie frames in the supporting information (**Figure S13**). If the peroxo species is not close to $Cl_{vac}$, the peroxo species needs to diffuse along the surface to approach $Cl_{vac}$. In this diffusion process[51] the top O atom of the peroxo species hops to a neighboring lattice O site forming a new peroxo species with a barrier of 1.23 eV (**Figure S14**, no $V_{O,SSS}$ in the slab). Both barriers can readily be overcome at 700 K. This structure diffusion process is reminiscent of the diffusion of protons in water (Grotthuss mechanism).

If more than two $Cl_{top}$ species form at the surface, they can recombine and the $Cl_2$ is released directly into the gas phase. According to DFT calculations this association step of two $Cl_{top}$ is activated by 0.87 eV and is endothermic by 0.79 eV (cf. **Figure 9**).
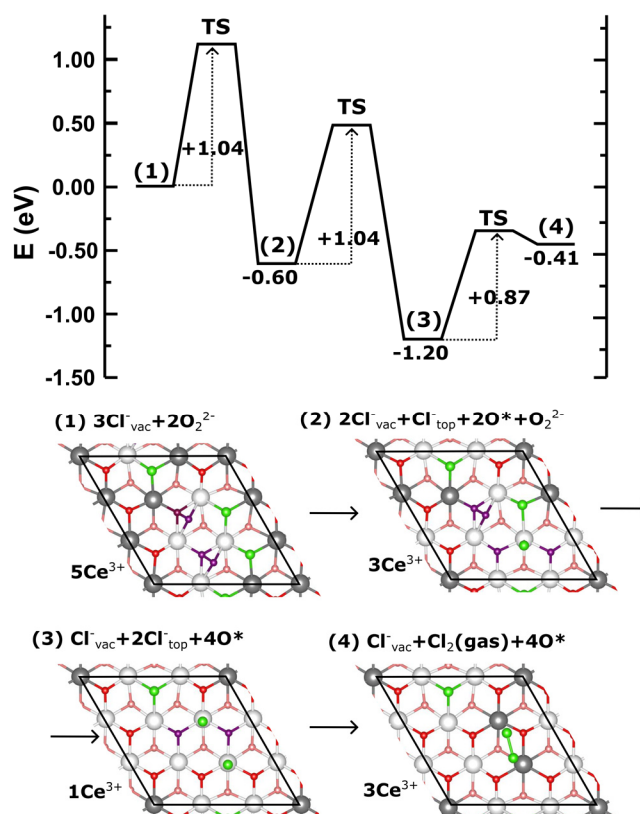
**Figure 9.** De-chlorination process of $3Cl_{vac}$-$Ce_3O_5(111)$-$(3 \times 3)$. Two peroxo species at the surface displace $Cl_{vac}$ to the $Cl_{top}$. This concerted process is activated by 1.04 eV and is exothermic by 0.6 eV. Subsequently, the two $Cl_{top}$ species recombine to form the desired product $Cl_2$. Color code: $Ce^{4+}$ are white and $Ce^{3+}$ atoms are gray, the oxygen surface (subsurface) atoms are red (light red), and Cl atoms are in green. The adsorbed $O_2^{2-}$ species are depicted in violet. O* indicates the lattice oxygen atoms that formed after $O_2^{2-}$ dissociation.

These DFT calculations can readily explain the experiments presented in section 3.2. The activation energy for the bulk re-oxidation is governed by the diffusion barrier of O vacancies from the bulk towards the surface (0.80 eV), while the activation barrier for the displacement step $Cl_{vac} \rightarrow Cl_{top}$ is 1.04 eV. From this difference in activation energies, the branching ratio at 700 K between these competing reactions is inferred to be about 1:50 in favor of bulk re-oxidation. This is fully consistent with the experimental observation that the Cl 2p HRCL spectra (cf. **Figure 5**) are practically unaltered as long as the bulk $CeO_{2-x}(111)$ is not nearly fully re-oxidized (cf. bulk-sensitive XANES **Figure 3**).

When the bulk and the near surface region of $CeO_{2-x}(111)$ are essentially re-oxidized after exposing 300 L of $O_2$ at 700 K, the lifetime of the adsorbed peroxo species is long enough to induce the competing displacement reaction of $Cl_{vac} \rightarrow Cl_{top}$. Since the surface concentration of O vacancies ($V_{O,S}$) is expected to be small after bulk re-oxidation, only very few peroxo species are formed and as a consequence the displacement step $Cl_{vac} \rightarrow Cl_{top}$ is quite slow. The $Cl_{top}$ species is not long-lived on the surface since the recombination of two neighboring $Cl_{top}$ species to form $Cl_2$ gas is activated by only 0.87 eV and proceeds therefore rapidly at 700 K; recall the great entropy gain during desorption process. This explains also, why $Cl_{top}$ cannot be detected in the Cl 2p spectrum (cf. **Figure 5a**), thus supporting the interpretation of the observed shift in Cl 2p spectra being due to re-oxidation of the surface near region. After exposure of 2700 L $O_2$ the reduction in $Cl_{vac}$ coverage saturates and amounts to 25% (cf. **Figure 5b**). A possible explanation is that there are not enough oxygen vacancies available at the surface into which $O_2$ can adsorb as peroxo. This terminates the displacement reaction $Cl_{vac} \rightarrow Cl_{top}$ and the subsequent recombination step of neighboring $Cl_{top}$ species.

## 3.4 Removal of $Cl_{vac}$ by exposure to atomic O at 300 K and $O_2$ at 500 K

The DFT calculations in section 3.3 motivate further experiments. The low activation energies found by DFT calculations suggest that partial removal of $Cl_{vac}$ should even occur at 500 K. This set of experiments is presented in **Figure 10a**. Even at 500 K the Cl 2p signal decreases with $O_2$ exposure, although we need approximately 10 times higher $O_2$ doses in comparison with re-oxidation at 700 K. This is explainable since both the formation of surface vacancies and the displacement reaction are activated by 0.80 eV and 1.04 eV, respectively (cf. **Figures 8** and **9**).
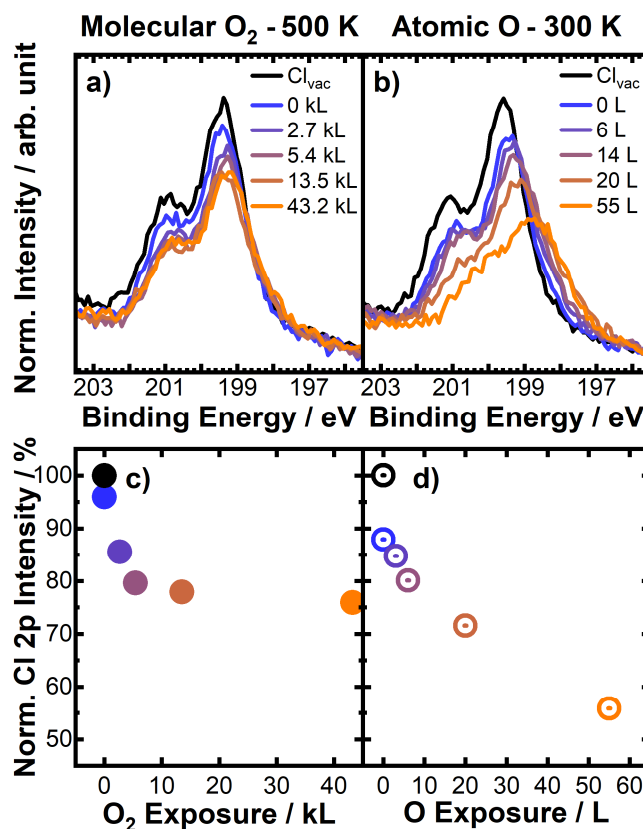


**Figure 10.** Cl 2p lab XP spectra: a) de-chlorination and re-oxidation at 500 K with 43.2kL $O_2$. b) de-chlorination and re-oxidation at 300 K with 55L atomic O, c) and d): integrated intensity of the Cl 2p peak of a) and b) respectively. Note that the exposures in panel c) are given in kL. Detector angle $\theta = 60°$ for enhanced surface sensitivity.

In order to stabilize the peroxo species upon $O_2$ exposure, we need the presence of oxygen vacancies at the surface ($V_{O,s}$). Since the concentration of surface oxygen vacancies after bulk re-oxidation of $Cl_{vac}$-$CeO_{2-x}(111)$ is very low, the peroxo species remains a kind of "ghost species" that is present only in spurious amounts, and it is easily consumed by re-oxidation and the displacement reaction. However, there is an alternative and efficient way to produce the peroxo species, namely by exposure to atomic oxygen O.[58] At room temperature, surface lattice $O^{2-}$ sites can be transformed to $O_2^{2-}$ by atomic O exposure without changing the oxidation state of Ce. Of course, atomic oxygen can also adsorb on surface Ce sites, but this adsorption process is by 0.48 eV less favorable than the adsorption on surface lattice O followed by the formation of $O_2^{2-}$ (cf. **Figure 7b**). The peroxo species in turn induces the shift of $Cl_{vac}$ species from the vacancy position to the top position $Cl_{top}$ where chlorine can subsequently recombine and desorb from the surface as $Cl_2$. In this way, part of the $Cl_{vac}$ at the surface can be removed by exposing the re-oxidized $Cl_{vac}$-$CeO_{2-x}(111)$ surface to atomic oxygen at 300 K while monitoring the Cl 2p signal. From this set of experiments summarized in **Figure 10b** it is clear that low exposures of ~50 L O are sufficient to remove half of the surface $Cl_{vac}$ species, which,

14

in turn, corroborates the preferential formation of peroxo species and its important role in the $Cl_{vac} \rightarrow Cl_{top}$ displacement reaction. The peroxo species on the stoichiometric $CeO_2(111)$ can also be verified in the O 1s spectrum (cf. **Figure S15**). The O 1s component at 531.3 eV can clearly be discriminated from the OH species at 532.2 eV (cf. **Figure S6**) and according to a recent XPS study the low energy component was assigned to the peroxo species based on DFT-derived binding energy shifts.[58]

## 4. Discussion

### 4.1 Catalytically active surface of CeO₂ under typical Deacon reaction conditions

The Deacon reaction with $CeO_2$ as catalyst typically runs under oxidizing reaction conditions (feed $O_2$ : HCl > 1:4) as the reaction order of $O_2$ is positive.[1] Nevertheless, $CeO_2$ can be reduced in oxidizing reaction mixtures, which stabilizes strongly adsorbing chlorine at the surface.[10,59−61] This reduction is enabled by HCl adsorbing in an acid-base reaction leading towards OH group formation on surface lattice O and Cl atom adsorption on surface Ce. With high enough temperature chlorine atoms are able to recombine to form $Cl_2$ whereas neighboring OH groups are able to form water and an oxygen vacancy upon recombination. The formed oxygen vacancy can be occupied by chlorine upon dissociative HCl adsorption or by peroxo species. Note that the peroxo species can desorb at 700 K and the further dissociation of peroxo would need another subsurface O vacancy in its proximity. For kinetic reasons, chlorine adsorption is preferred over peroxo adsorption, leading to an accumulation of chlorine in surface oxygen vacancies. Ultimately, this will chlorinate the $CeO_{2−x}$ surface, where chlorine is strongly adsorbed in surface oxygen vacancies as $Cl_{vac}$.

Previously the chlorination degree of $CeO_2$ powder was quantified to be less than 1 ML (ML: monolayer) in an experiment with Prompt Gamma-ray Neutron Activation Analysis (PGAA).[59] Much closer to our model system are shape-controlled $CeO_2$ octahedrons exposing (111) facets.[62] After HCl oxidation reaction of $CeO_2$ nano-octahedrons with an oxidizing reaction feed $O_2$ : HCl = 2:1 (cf. stoichiometric feed: $O_2$ : HCl = 1:4), a mean $Ce^{3+}$ fraction of 29% in the near-surface region and a Cl/Ce ratio of 15% was determined.[60] The fresh $CeO_2$ catalyst possesses a $Ce^{3+}$ fraction of only 20%. From these experiments, the chlorine coverage can be estimated to be about 0.4 ML that would account for 9% of the $Ce^{3+}$; recall that each $Cl^−$ needs one $Ce^{3+}$ for charge compensation. Therefore, the residual 20% of $Ce^{3+}$ needs to be compensated by 10% oxygen vacancies. From the observation of a $(\sqrt{3} \times \sqrt{3})R30°$ pattern in LEED,[10] the Cl coverage is either 1/3 or 2/3, in broad agreement with the coverage estimated for $CeO_2$ nano-octahedrons.[60] In conclusion, this experimental evidence from powder and nanoparticle $CeO_2$ renders a chlorinated $CeO_{2−x}(111)$ surface with a $Cl_{vac}$ coverage of 1/3 and 10% oxygen vacancies a suitable model system for studying the elementary steps in the re-oxidation reaction as part of the Deacon process.

That the partially reduced $Cl_{vac}$-$CeO_{2−x}(111)$ surface is the active phase for the Deacon process is also consistent with previous studies showing that neither the stoichiometric[13] nor the deeply reduced $CeO_{2−x}(111)$ surfaces[10] are (very) active in the HCl oxidation reaction. The stoichiometric $CeO_2(111)$ surface leads preferentially to re-combinative desorption of HCl instead of $Cl_2$ formation, whereas the strongly reduced $CeO_{2−x}(111)$ surface binds chlorine in vacancy positions too strongly, thus suppressing direct $Cl_2$ evolution at 700 K. But also the water formation step needs a partially reduced $CeO_{2−x}(111)$ surface. On stoichiometric $CeO_2(111)$, water formation is not observed,[13] whereas on the reduced $CeO_{2−x}(111)$ surface, water formation is observed at 620 K,[10] if the $Ce^{3+}$ fraction (reduction degree $x$) of $CeO_{2−x}(111)$ is not too high.

With pure HCl exposure a reduced $CeO_{2−x}(111)$ surface may be completely covered by chlorine in vacancies. From an energy point of view a $(1 \times 1)$-$Cl_{vac}$ overlayer would be feasible as shown

15

by the differential heat of adsorption in **Figure S16**. A complete chlorination of the $CeO_{2-x}(111)$ surface would, however, de-activate the surface since neither $O_2$ nor HCl can further adsorb on this surface termination. Therefore, the oxygen-induced de-chlorination is important to prevent the $CeO_{2-x}(111)$ catalyst from over-chlorination of the $CeO_{2-x}(111)$ surface close to 1 ML and thus from de-activation.

### 4.2 Deacon reaction over $Cl_{vac}$-$CeO_{2-x}(111)$

The Deacon reaction can be broken down into two separate processes in which the catalyst undergoes a solid state redox cycle.[2,4,63] This separation in partial reactions can also be utilized in chemical looping.[64,65] First, HCl reduces the oxide catalyst to a (surface) chloride, during which water is formed as couple-product. This chlorination process is exothermic. In the second step the chlorinated surface is re-oxidized by molecular oxygen to recover the active phase of the catalyst, thereby releasing the desired $Cl_2$ and closing the catalytic cycle. This re-oxidation process can be considered as an oxygen-driven de-chlorination step, a process that is endothermic and that is in the focus of the present study starting from $Cl_{vac}$-$CeO_{2-x}(111)$. In **Figure 1**, all steps in the blue background comprises the chlorination process, while the steps with orange background belong to the de-chlorination process.

Amrute et al.[1] have introduced the $Cl_{vac}$ to $Cl_{top}$ displacement as critical step in the de-chlorination process of the ceria catalyst. They proposed that one of the oxygen atoms in the subsurface layer can diffuse toward the surface, pushing a $Cl_{vac}$ atom towards the top site on Ce and leaving one oxygen vacancy in the subsurface region. This step has been considered rate limiting for the Deacon process and is endothermic by 2.15 eV.[1] The following surface re-oxidation step has remained, however, largely elusive and was proposed to be carried out through "a complex diffusion-reaction mechanism"[1] that would release nearly 3.4 eV. Altogether, this combined process of oxidative displacement is exothermic by 1.2 eV; a lower energy of 0.53 eV was reported by Wolf et al.[66] consistent with the present DFT study.

With a combination of in-situ synchrotron-based techniques (XANES and HRCLS) the re-oxidation is shown to start from the bulk of $Cl_{vac}$-$CeO_{2-x}(111)$ and then propagates towards the surface. From bulk-sensitive XANES experiment (cf. **Figure 2**) the re-oxidation of bulk $CeO_{2-x}(111)$ is shown to proceed nearly linearly with $O_2$ exposure up to 300 L of $O_2$ and above 300 L the re-oxidation is significantly slowed down. Quite in contrast, the surface sensitive Ce 4d XP spectra (cf. **Figure 4**) indicate only little change of the $Ce^{3+}$ fraction in the surface region up to 200 L of $O_2$, while oxidation in the near surface region is then practically completed for exposures up to 300 L. Above 200L $O_2$ also Cl 2p spectra (cf. **Figure 5**) alter in that the spectral features shift slightly to lower binding energies and the integral intensity starts to decrease with $O_2$ exposure. We do not directly observe the actual activation step from $Cl_{vac}$ to $Cl_{top}$, but instead monitor with the Cl 2p spectra the oxygen-driven removal of $Cl_{vac}$, i.e. the partial de-chlorination of the $Cl_{vac}$-$CeO_{2-x}(111)$ surface, by the recombination of $Cl_{top}$ species to form $Cl_2$ and its instant release to the gas phase at 700 K.

These experiments are fully explained by the present DFT study. The most important reaction intermediate for the re-oxidation and de-chlorination of $Cl_{vac}$-$CeO_{2-x}(111)$ turns out to be the peroxo species ($O_2^{2-}$) that is stabilized into surface oxygen vacancies by ~2 eV, in agreement with the previous theoretical works.[51,67–69] Whenever an additional vacancy appears in the subsurface region directly below the peroxo species, the peroxo species dissociates and replenishes two oxygen vacancies. From the calculated activation energies bulk re-oxidation (0.80 eV) precedes the $Cl_{vac} \rightarrow Cl_{top}$ displacement step (1.04 eV). The recombination of two $Cl_{top}$ species to form $Cl_2$ is activated by 0.87 eV that results in its instant release to the gas phase at 700 K. The $Cl_{vac} \rightarrow Cl_{top}$ displacement step is demonstrated to be directly coupled with the surface re-oxidation step that is induced by a neighboring peroxo species. This makes the concerted displacement step exothermic by 0.6 eV with an activation energy of about 1 eV.

16

A de-chlorination experiment with atomic oxygen O provides indirect experimental evidence for the important role of the peroxo species in the de-chlorination process. Atomic O exposure is able to form peroxo species at the surface without the need of surface O-vacancies.[58] Indeed experiments in **Figure 10b** indicate that room temperature exposure of ~50 L of atomic O is able to remove 40% of $Cl_{vac}$ from the surface, a larger portion than that achieved by exposure of 2700 L of $O_2$ at 700 K (25%).

## 4.3 Peroxo species is essential for oxidation catalysis over $CeO_2$

The ability to remove/uptake oxygen from the lattice while maintaining structural integrity endows ceria with unique properties in catalysis science and technology.[42,70] The mass-specific amount of oxygen that can be exchanged with the oxide catalyst is called the oxygen storage capacity (OSC).[71,72] The $O_2$ incorporation requires two oxygen vacancies and electrons supplied from the oxidation of $Ce^{3+}$.[73] Frequently, the OSC serves as a simple descriptor for the activity in oxidation catalysis of reducible oxides.[9,74–77] Oxygen vacancies are considered mandatory for catalysis on ceria.[78–80]

On the basis of previous spectroscopic experiments on $CeO_2$ powders[81–86] and $CeO_{2-x}(111)$ platelets,[69] superoxo- and peroxo species have been identified and assumed to play an important role in the oxidation chemistry of ceria. In the present study we show that the adsorption energy of peroxo species at O-vacancies of $CeO_{2-x}(111)$ is quite high (~2 eV). Therefore, the peroxo species has a long lifetime on the surface even at high temperatures of 700 K. For the re-oxidation of $CeO_{2-x}$, we do not need to assume two neighboring surface O vacancy sites for direct $O_2$ dissociation. Instead, the re-oxidation process can take place in two consecutive steps, namely the activation of $O_2$ gas to form the peroxo species at the surface oxygen vacancy $V_{O,S}$ and its dissociation as soon as another subsurface O vacancy approaches the peroxo species. Therefore, the peroxo species is mandatory for the oxygen storage capacity (OSC).[71,72]

A combination of infrared vibrational spectroscopy and DFT calculations[68] demonstrated that the activation of $O_2$ at vacancies on single crystalline $CeO_{2-x}(100)$ and $CeO_{2-x}(110)$ takes place via peroxo and superoxo species, but not on $CeO_{2-x}(111)$. The main reason for this apparent discrepancy with the present study is the low adsorption temperature of 110 K in Ref.[68] For such low temperatures, oxygen vacancies of $CeO_{2-x}(111)$ are frozen in the subsurface region and are not accessible to $O_2$ adsorption from the gas phase. In our case $O_2$ adsorption takes place at higher temperatures and therefore oxygen vacancies, although with low concentration, are available on the surface of $CeO_{2-x}(111)$.

The peroxo group at the surface can diffuse across the surface. In fact, not the whole peroxo species diffuses, but rather the upper O atom of $O_2^{2-}$ diffuses to the neighboring surface lattice O site and transforms it into another peroxo species. With an activation energy of 1.2 eV, this barrier can easily be overcome at 500−700 K, making the peroxo species a mobile surface species. For supported catalysts with $CeO_2$ being the carrier, the mobility of this peroxo species will be important for facile oxygen exchange between the active particle and the $CeO_2$ support in the form of spill-over and back spill-over species.

Superoxide ($O_2^-$) and peroxide (peroxo: $O_2^{2-}$) are known to be important oxygen species in catalytic oxidation reactions[87] on ceria-based catalysts that were studied both experimentally and theoretically (see, e.g., Ref.[52,56,87–97]). In this work, we demonstrate the crucial role of the peroxo species in the HCl oxidation reaction during the de-chlorination process. The peroxo species induces the displacement of Cl from the vacancy position ($Cl_{vac}$) towards the on-top position ($Cl_{top}$) and the subsequent desorption in the form of $Cl_2$. The concerted displacement of Cl maintains the oxidation state of −1, while the desorption step leads to the oxidation of chlorine towards zero oxidation state. Concerted displacement of reaction intermediates may be important in oxidation catalysis over ceria.

17

## 5. Conclusion

During the HCl oxidation reaction ceria catalysts undergo a redox cycle and their catalytic activity is governed by the ease with which the chlorinated $CeO_{2-x}$ surfaces can be de-chlorinated by oxygen exposure, thereby releasing the desired product $Cl_2$. Based on a previous DFT study, the displacement step of $Cl_{vac}$ species towards $Cl_{top}$ was predicted to be the critical reaction step in the HCl oxidation activity of ceria.[1] Unfortunately, this displacement step is highly endothermic.[1] Synchrotron-based methods, including in situ X-ray absorption spectroscopy (XANES) and in situ high-resolution core level shift spectroscopy (HRCLS), together with first principles DFT calculations are employed to elucidate this critical reaction step in the HCl oxidation reaction with a dedicated model experiment, namely the re-oxidation of a chlorinated single crystalline $CeO_{2-x}(111)$ model catalyst at 700 K, a typical reaction temperature for the HCl oxidation reaction. The synchrotron photon energies in HRCLS are carefully chosen to be highly surface sensitive, while Ce $M_{4,5}$ edge XANES (Ce 3d) in total electron yield probes bulk properties. With this combination of surface and bulk sensitive methods, we demonstrate that the re-oxidation of the chlorinated $CeO_{2-x}(111)$ surface at 700 K starts from the bulk and propagates subsequently towards the surface. The re-oxidation of $Cl_{vac}$-$CeO_{2-x}(111)$ considerably weakens the adsorption energy of the $Cl_{vac}$ species. Ultimately, part of the $Cl_{vac}$ species are shifted to on-top positions $Cl_{top}$, where they recombine to form $Cl_2$. Both the re-oxidation of $CeO_{2-x}(111)$ and the $Cl_{vac} \rightarrow Cl_{top}$ displacement step of surface chlorine are predicted by DFT calculations to be induced by peroxo species ($O_2^{2-}$). In this way the displacement step and surface re-oxidation are coupled so that the concerted displacement step becomes now exothermic by 0.6 eV with an activation barrier of about ~1 eV. With such a low activation barrier the $Cl_{vac} \rightarrow Cl_{top}$ site change is shown to take place even at 500 K, although requiring a higher $O_2$ exposure than for the 700 K re-oxidation. The peroxo species do not only impact the Deacon process, but are of general importance for catalytic oxidation reactions on $CeO_2$ supported catalysts. Oxygen spill-over effects for supported particles on $CeO_2$ are intimately correlated with the peroxo species and their facile (structure) diffusion across the surface.

## Supporting Information

- X-ray reflectivity data;
- LEED patterns of $CeO_{2-x}(111)$ and $Cl_{vac}$-$CeO_{2-x}(111)$;
- Decomposition of Ce $M_{4,5}$ edge XANES of $CeO_{2-x}(111)$ by linear combination of $CeO_2(111)$ and $Ce_2O_3$ reference spectra;
- Decomposition of Ce 4d HRCL spectra of $CeO_{2-x}(111)$ by linear combination of $CeO_2(111)$ and $Ce_2O_3$ reference spectra;
- Cl 2p HRCL spectra during annealing step of $Cl_{vac}$-$CeO_{2-x}(111)$;
- O 1s HRCL spectra during annealing step of $Cl_{vac}$-$CeO_{2-x}(111)$;
- O 1s spectra of re-oxidation $Cl_{vac}$-$CeO_{2-x}(111)$;
- Ball and stick model of $Cl_{vac}$-$CeO_{2-x}(111)$;
- Deconvolution Cl 2p HRCL spectra: before and after re-oxidation;
- Cl 2p spectra of re-oxidation $Cl_{vac}$-$CeO_{2-x}(111)$ ($hv$ = 850 eV);
- Cl 2p spectra during flash off $Cl_{vac}$-$CeO_{2-x}(111)$;
- Energy diagram for different vacancy diffusion pathways;
- Movie frames of the de-chlorination process;
- Energy diagram and pathway for surface diffusion of peroxo species;
- O 1s spectrum of peroxo species on $CeO_2(111)$;
- Differential heat of adsorption of Cl;
- References with more than 10 authors;

**Data Availability**

The DFT data that support the findings of this study are available in Materials Cloud {https://www.materialscloud.org/home} with the identifier DOI: 10.24435/materialscloud:1b-0f. The data are also available from the authors upon reasonable request.

## References

(1) Amrute, A. P.; Mondelli, C.; Moser, M.; Novell-Leruth, G.; López, N.; Rosenthal, D.; Farra, R.; Schuster, M. E.; Teschner, D.; Schmidt, T., et al. Performance, Structure, and Mechanism of $CeO_2$ in HCl Oxidation to $Cl_2$. *J. Catal.* **2012**, *286*, 287–297.

(2) Hisham, M. W. M.; Benson, S. W. Thermochemistry of the Deacon Process. *J. Phys. Chem.* **1995**, *99*, 6194–6198.

(3) Pérez-Ramírez, J.; Mondelli, C.; Schmidt, T.; Schlüter, O. F.-K.; Wolf, A.; Mleczko, L.; Dreier, T. Sustainable Chlorine Recycling via Catalysed HCl Oxidation: From Fundamentals to Implementation. *Energy Environ. Sci.* **2011**, *4*, 4786–4799.

(4) Over, H.; Schomäcker, R. What Makes a Good Catalyst for the Deacon Process? *ACS Catal.* **2013**, *3*, 1034–1046.

(5) Deacon, H. Improvement in the Manufacture of Chlorine. US 0085370 A, 1868.

(6) Deacon, H. XXIX.—On Deacon's Method of Obtaining Chlorine, as Illustrating Some Principles of Chemical Dynamics. *J. Chem. Soc.* **1872**, *25*, 725–767.

(7) Seki, K. Development of $RuO_2$/Rutile-$TiO_2$ Catalyst for Industrial HCl Oxidation Process. *Catal. Surv. Asia* **2010**, *14*, 168–175.

(8) Moser, M.; Mondelli, C.; Schmidt, T.; Girgsdies, F.; Schuster, M. E.; Farra, R.; Szentmiklósi, L.; Teschner, D.; Pérez-Ramírez, J. Supported $CeO_2$ Catalysts in Technical Form for Sustainable Chlorine Production. *Appl. Catal., B* **2013**, *132-133*, 123–131.

(9) Capdevila-Cortada, M.; Vilé, G.; Teschner, D.; Pérez-Ramírez, J.; López, N. Reactivity Descriptors for Ceria in Catalysis. *Appl. Catal., B* **2016**, *197*, 299–312.

(10) Koller, V.; Sack, C.; Lustemberg, P.; Ganduglia-Pirovano, M.V.; Over, H. Dynamic Response of Oxygen Vacancies in the Deacon Reaction over Reduced Single Crystalline $CeO_{2-x}$(111) surface. *J. Phys. Chem. C* **2022**, *126*, 13202–13212.

(11) Over, H.; Bludau, H.; Skottke-Klein, M.; Ertl, G.; Moritz, W.; Campbell, C. T. Coverage Dependence of Adsorption-Site Geometry in the Cs/Ru(0001) System: A Low-Energy Electron-Diffraction Analysis. *Phys. Rev. B: Condens. Matter Mater. Phys.* **1992**, *45*, 8638–8649.

(12) Hofmann, J. P.; Rohrlack, S. F.; Heß, F.; Goritzka, J. C.; Krause, P. P.; Seitsonen, A. P.; Moritz, W.; Over, H. Adsorption of Chlorine on Ru(0001)—A Combined Density Functional Theory and Quantitative Low Energy Electron Diffraction Study. *Surf. Sci.* **2012**, *606*, 297–304.

(13) Sack, C.; Lustemberg, P.; Koller, V.; Ganduglia-Pirovano, M. V.; Over, H. Interaction of HCl with a $CeO_2$(111) Layer Supported on Ru(0001): A Theory and Experiment Combined Study. *J. Phys. Chem. C* **2018**, *122*, 19584–19592.

(14) Mullins, D. R.; Radulovic, P. V.; Overbury, S. H. Ordered Cerium Oxide Thin Films Grown on Ru(0001) and Ni(111). *Surf. Sci.* **1999**, *429*, 186–198.

(15) Hasegawa, T.; Shahed, S. M. F.; Sainoo, Y.; Beniya, A.; Isomura, N.; Watanabe, Y.; Komeda, T. Epitaxial Growth of $CeO_2$(111) Film on Ru(0001): Scanning Tunneling Microscopy (STM) and X-Ray Photoemission Spectroscopy (XPS) Study. *J. Chem. Phys.* **2014**, *140*, 044711.

(16) Schierbaum, K.-D. Ordered Ultra-Thin Cerium Oxide Overlayers on Pt(111) Single Crystal Surfaces Studied by LEED and XPS. *Surf. Sci.* **1998**, *399*, 29–38.

(17) Lu, J.-L.; Gao, H.-J.; Shaikhutdinov, S.; Freund, H.-J. Morphology and Defect Structure of the $CeO_2$(111) Films Grown on Ru(0001) as Studied by Scanning Tunneling Microscopy. *Surf. Sci.* **2006**, *600*, 5004–5010.

(18) Kaemena, B.; Senanayake, S. D.; Meyer, A.; Sadowski, J. T.; Falta, J.; Flege, J. I. Growth and Morphology of Ceria on Ruthenium (0001). *J. Phys. Chem. C* **2013**, *117*, 221–232.

(19) Stetsovych, V.; Pagliuca, F.; Dvořák, F.; Duchoň, T.; Vorokhta, M.; Aulická, M.; Lachnitt, J.; Schernich, S.; Matolínová, I.; Veltruská, K., et al. Epitaxial Cubic $Ce_2O_3$ Films via Ce-$CeO_2$ Interfacial Reaction. *J. Phys. Chem. Lett.* **2013**, *4*, 866–871.

(20) Höcker, J.; Krisponeit, J.-O.; Schmidt, T.; Falta, J.; Flege, J. I. The Cubic-to-Hexagonal Phase Transition of Cerium Oxide Particles: Dynamics and Structure. *Nanoscale* **2017**, *9*, 9352–9358.

(21) Preobrajenski, A.; Generalov, A.; Öhrwall, G.; Tchaplyguine, M.; Tarawneh, H.; Appelfeller, S.; Frampton, E.; Walsh, N. FlexPES: a Versatile soft X-ray Beamline at MAX IV Laboratory. *J. Synchrotron Radiat.* **2023**, *30*, 831–840.

(22) Duchoň, T.; Dvořák, F.; Aulická, M.; Stetsovych, V.; Vorokhta, M.; Mazur, D.; Veltruská, K.; Skála, T.; Mysliveček, J.; Matolínová, I., et al. Ordered Phases of Reduced Ceria as Epitaxial Films on Cu(111). *J. Phys. Chem. C* **2014**, *118*, 357–365.

(23) Dvořák, F.; Szabová, L.; Johánek, V.; Farnesi Camellone, M.; Stetsovych, V.; Vorokhta, M.; Tovt, A.; Skála, T.; Matolínová, I.; Tateyama, Y., et al. Bulk Hydroxylation and Effective Water Splitting by Highly Reduced Cerium Oxide: The Role of O Vacancy Coordination. *ACS Catal.* **2018**, *8*, 4354–4363.

(24) Seah, M.P.; Dench, W.A. Quantitative Electron Spectroscopy of Surfaces: A Standard Data Base for Electron Inelastic Mean Free Paths in Solids. *Surf. Interface Anal.* **1979,** *1*, 2–11.

(25) Cooper, J.W. Photoionization from Outer Atomic Subshells. A Model Study, *Phys. Rev.* **1962**, *128*, 681–693.

(26) Yeh, J. J.; Lindau, I. Atomic Subshell Photoionization Cross Sections and Asymmetry Parameters: $1 \leqslant Z \leqslant 103$. *At. Data Nucl. Data Tables* **1985**, *32*, 1–155.

(27) Payne, M. C.; Teter, M. P.; Allan, D. C.; Arias, T. A.; Joannopoulos, J. D. Iterative Minimization Techniques for Ab Initio Total-Energy Calculations: Molecular Dynamics and Conjugate Gradients. *Rev. Mod. Phys.* **1992**, *64*, 1045–1097.

(28) Kresse, G.; Hafner, J. Ab Initio Molecular Dynamics for Liquid Metals. *Phys. Rev. B: Condens. Matter Mater. Phys.* **1993**, *47*, 558–561.

(29) Kresse, G.; Hafner, J. Ab Initio Molecular-Dynamics Simulation of the Liquid-Metal-Amorphous-Semiconductor Transition in Germanium. *Phys. Rev. B: Condens. Matter Mater. Phys.* **1994**, *49*, 14251–14269.

(30) Kresse, G.; Furthmüller, J. Efficiency of Ab-Initio Total Energy Calculations for Metals and Semiconductors Using a Plane-Wave Basis Set. *Comput. Mater. Sci.* **1996**, *6*, 15–50.

(31) Kresse, G.; Furthmüller, J. Efficient Iterative Schemes for Ab Initio Total-Energy Calculations Using a Plane-Wave Basis Set. *Phys. Rev. B: Condens. Matter Mater. Phys.* **1996**, *54*, 11169–11186.

(32) Kresse, G.; Joubert, D. From Ultrasoft Pseudopotentials to the Projector Augmented-Wave Method. *Phys. Rev. B: Condens. Matter Mater. Phys.* **1999**, *59*, 1758–1775.

(33) Blöchl, P. E. Projector Augmented-Wave Method. *Phys. Rev. B: Condens. Matter Mater. Phys.* **1994**, *50*, 17953–17979.

(34) Dudarev, S. L.; Botton, G. A.; Savrasov, S. Y.; Humphreys, C. J.; Sutton, A. P. Electron-Energy-Loss Spectra and the Structural Stability of Nickel Oxide: An LSDA+U Study. *Phys. Rev. B: Condens. Matter Mater. Phys.* **1998**, *57*, 1505–1509.

(35) Perdew, J. P.; Burke, K.; Ernzerhof, M. Generalized Gradient Approximation Made Simple. *Phys. Rev. Lett.* **1996**, *77*, 3865–3868.

(36) Olbrich, R.; Murgida, G. E.; Ferrari, V.; Barth, C.; Llois, A. M.; Reichling, M.; Ganduglia-Pirovano, M. V. Surface Stabilizes Ceria in Unexpected Stoichiometry. *J. Phys. Chem. C* **2017**, *121*, 6844–6851.

(37) Monkhorst, H. J.; Pack, J. D. Special Points for Brillouin-Zone Integrations. *Phys. Rev. B* **1976**, *13*, 5188–5192.

(38) Henkelman, G.; Uberuaga, B. P.; Jónsson, H. A Climbing Image Nudged Elastic Band Method for Finding Saddle Points and Minimum Energy Paths. *J. Chem. Phys.* **2000**, *113*, 9901–9904.

(39) Kaindl, G.; Kalkowski, G.; Brewer, W. D.; Perscheid, B.; Holtzberg, F. *M*-edge X-ray Absorption Spectroscopy of 4*f* Instabilities in Rare-earth Systems (Invited). *J. Appl. Phys.* **1984**, *55*, 1910–1915.

(40) Yagci, O. The $M_{4,5}$ Photo-Absorption Spectra of Cerium in $CeO_2$ and Oxidation of Metallic Cerium. *J. Phys. C: Solid State Phys.* **1986**, *19*, 3487–3495.

(41) Mullins, D.; Overbury, S.; Huntley, D. Electron Spectroscopy of Single Crystal and Polycrystalline Cerium Oxide Surfaces. *Surf. Sci.* **1998**, *409*, 307–319.

(42) Mullins, D. R. The Surface Chemistry of Cerium Oxide. *Surf. Sci. Rep.* **2015**, *70*, 42–85.

(43) Hackl, J.; Duchoň, T.; Gottlob, D. M.; Cramm, S.; Veltruská, K.; Matolín, V.; Nemšák, S.; Schneider, C. M. On the Growth Mechanisms of Polar (100) Surfaces of Ceria on Copper (100). *Surf. Sci.* **2018**, *671*, 1–5.

(44) Crihan, D.; Knapp, M.; Zweidinger, S.; Lundgren, E.; Weststrate, C. J.; Andersen, J. N.; Seitsonen, A. P.; Over, H. Stable Deacon Process for HCl Oxidation over $RuO_2$. *Angew. Chem., Int. Ed.* **2008**, *47*, 2131–2134.

(45) Mullins, D.R.; Albrecht, P.M.; Chen, T.L.; Calaza, F.C.; Biegalski, M.D.; Christen, H.M.; Overbury, S.H. Water Dissociation on $CeO_2(100)$ and $CeO_2(111)$ Thin Films. *J. Phys. Chem. C* **2012**, *116*, 19419–19428.

(46) Liu, Z.; Grinter, D. C.; Lustemberg, P. G.; Nguyen-Phan, T.-D.; Zhou, Y.; Luo, S.; Waluyo, I.; Crumlin, E. J.; Stacchiola, D. J.; Zhou, J., et al. Dry Reforming of Methane on a Highly-Active Ni-$CeO_2$ Catalyst: Effects of Metal-Support Interactions on C-H Bond Breaking. *Angew. Chem., Int. Ed.* **2016**, *55*, 7455–7459.

(47) Posada-Borbón, A.; Bosio, N.; Grönbeck, H. On the Signatures of Oxygen Vacancies in O1s Core Level Shifts. *Surf. Sci.* **2021**, *705*, 121761.

(48) Hofmann, J. P.; Zweidinger, S.; Seitsonen, A. P.; Farkas, A.; Knapp, M.; Balmes, O.; Lundgren, E.; Andersen, J. N.; Over, H. Dynamic Response of Chlorine Atoms on a $RuO_2(110)$ Model Catalyst Surface. *Phys. Chem. Chem. Phys.* **2010**, *12*, 15358–15366.

(49) Hofmann, J. P.; Zweidinger, S.; Knapp, M.; Seitsonen, A. P.; Schulte, K.; Andersen, J. N.; Lundgren, E.; Over, H. Hydrogen-Promoted Chlorination of $RuO_2$ (110). *J. Phys. Chem. C* **2010**, *114*, 10901–10909.

(50) Murgida, G. E.; Ferrari, V.; Llois, A. M.; Ganduglia-Pirovano, M. V. Reduced $CeO_2(111)$ Ordered Phases as Bulk Terminations: Introducing the Structure of $Ce_3O_5$. *Phys. Rev. Mater.* **2018**, *2*, 083609.

(51) Huang, M.; Fabris, S. Role of Surface Peroxo and Superoxo Species in the Low-Temperature Oxygen Buffering of Ceria: Density Functional Theory Calculations. *Phys. Rev. B* **2007**, *75*, 081404(R).

(52) Zhao, Y.; Teng, B.-T.; Wen, X.-D.; Zhao, Y.; Chen, Q.-P.; Zhao, L.-H.; Luo, M.-F. Superoxide and Peroxide Species on $CeO_2(111)$, and Their Oxidation Roles. *J. Phys. Chem. C* **2012**, *116* (30), 15986–15991.

(53) Ganduglia-Pirovano, M. V.; Da Silva, J. L. F.; Sauer, J. Density-functional Calculations of the Structure of Near-surface Oxygen Vacancies and Electron Localization on $CeO_2(111)$. *Phys. Rev. Lett.* **2009**, *102*, 26101.

(54) Murgida, G. E.; Ganduglia-Pirovano, M. V. Evidence for Subsurface Ordering of Oxygen Vacancies on the Reduced $CeO_2(111)$ Surface Using Density-functional and Statistical Calculations. *Phys. Rev. Lett.* **2013**, *110*, 246101.

(55) Zhang, D.; Han, Z.-K.; Murgida, G. E.; Ganduglia-Pirovano, M. V.; Gao, Y. Oxygen-Vacancy Dynamics and Entanglement with Polaron Hopping at the Reduced $CeO_2(111)$ Surface. *Phys. Rev Lett.* **2019**, *122*, 96101.

(56) Preda, G.; Pacchioni, G. Formation of Oxygen Active Species in Ag-modified $CeO_2$ Catalyst for Soot Oxidation: A DFT study. *Catal. Tod.* **2011**, *177*, 31–38.

(57) Lykhach, Y.; Kozlov, S. M.; Skála, T.; Tovt, A.; Stetsovych, V.; Tsud, N.; Dvořák, F.; Johánek, V.; Neitzel, A.; Mysliveček, J., et al. Counting Electrons on Supported Nanoparticles. *Nat. Mater.* **2016**, *15*, 284–288.

(58) Wan, W.; Geiger, J.; Berdunov, N.; Lopez Luna, M.; Chee, S. W.; Daelman, N.; López, N.; Shaikhutdinov, S.; Roldan Cuenya, B. Highly Stable and Reactive Platinum Single Atoms on Oxygen Plasma-Functionalized $CeO_2$ Surfaces: Nanostructuring and Peroxo Effects. *Angew. Chem., Int. Ed.* **2022**, *61*, e202112640.

(59) Farra, R.; Eichelbaum, M.; Schlögl, R.; Szentmiklósi, L.; Schmidt, T.; Amrute, A. P.; Mondelli, C.; Pérez-Ramírez, J.; Teschner, D. Do Observations on Surface Coverage-Reactivity Correlations Always Describe the True Catalytic Process? A Case Study on Ceria. *J. Catal.* **2013**, *297*, 119–127.

(60) Li, C.; Sun, Y.; Djerdj, I.; Voepel, P.; Sack, C.-C.; Weller, T.; Ellinghaus, R.; Sann, J.; Guo, Y.; Smarsly, B. M., et al. Shape-Controlled $CeO_2$ Nanoparticles: Stability and Activity in the Catalyzed HCl Oxidation Reaction. *ACS Catal.* **2017**, *7*, 6453–6463.

(61) Sun, Y.; Hess, F.; Djerdj, I.; Wang, Z.; Weber, T.; Guo, Y.; Smarsly, B. M.; Over, H. Reactivation of $CeO_2$-based Catalysts in the HCl Oxidation Reaction: In situ Quantification of the Degree of Chlorination and Kinetic Modeling. *ChemCatChem* **2020**, *12*, 5511–5522.

(62) Trovarelli, A.; Llorca, J. Ceria Catalysts at Nanoscale: How do Crystal Shapes Shape Catalysis? *ACS Catal.* **2017**, *7*, 4716–4735.

(63) Allen, J. A. Energetic Criteria for Oxychlorination Catalysts. *J. Appl. Chem. (London, U. K.)* **1962**, *12*, 406–412.

(64) Zeng, L.; Cheng, Z.; Fan, J.A.; Fan, L.S.; Gong, J.L. Metal Oxide Redox Chemistry for Chemical Looping Processes. *Nat. Rev. Chem.* **2018**, *2*, 349–364.

(65) Metcalfe, I.S.; Ray, B.; Dejoie, C.; Hu, W.; de Leeuwe, C.; Dueso, C.; Garcia-Garcia, F.R.; Mak, C.-M.; Papaioannou, E.I.; Thompson, C.R., et al. Overcoming Chemical Equilibrium Limitations Using a Thermodynamically Reversible Chemical Reactor. *Nat. Chem.* **2019**, *11*, 638–643.

(66) Wolf, M.J.; Larsson, E.D.; Hermansson, K. Oxygen Chemistry of Halogen-Doped $CeO_2(111)$. *Phys. Chem. Chem. Phys.* **2021**, *23*, 19375–19385.

(67) Paier, J.; Penschke, C: Sauer, J. Oxygen Defects and Surface chemistry of Ceria: Quantum chemical Studies Compared to Experiment. *Chem. Rev.* **2013**, *113*, 3949–3985.

(68) Yang, C.; Yu, X.; Heißler, S.; Weidler, P. G.; Nefedov, A.; Wang, Y.; Wöll, C.; Kropp, T.; Paier, J.; Sauer, J. $O_2$ Activation on Ceria Catalysts – The Importance of Substrate Crystallographic Orientation. *Angew. Chem., Int. Ed.* **2017**, *56*, 16399–16404.

(69) Schilling, C.; Ganduglia-Pirovano, M. V.; Hess, C. Experimental and Theoretical Study on the Nature of Adsorbed Oxygen Species on Shaped Ceria Nanoparticles. *J. Phys. Chem. Lett.* **2018**, *9*, 6593–6598.

(70) *Catalysis by Ceria and Related Materials, 2nd edition*; Trovarelli, A., Fornasiero, P., Eds.; Imperial College Press: London, U.K., 2013.

(71) Yao, H. C.; Yao, Y. F. Y. Ceria in Automotive Exhaust Catalysts: I. Oxygen Storage. *J. Catal.* **1984**, *86*, 254–265.

(72) Li, P.; Chen, X.; Li, Y.; Schwank, J. W. A Review on Oxygen Storage Capacity of $CeO_2$-Based Materials: Influence Factors, Measurement Techniques, and Applications in Reactions Related to Catalytic Automotive Emissions Control. *Catal. Today* **2019**, *327*, 90–115.

(73) Maier, J. *Physical Chemistry of Ionic Materials*: *Ions and Electrons in Solids*; John Wiley & Sons, Ltd: Chichester, England, 2004.

(74) Grasselli, R. K. Fundamental Principles of Selective Heterogeneous Oxidation Catalysis. *Top. Catal.* **2002**, *21*, 79–88.

(75) Wachs, I. E. Recent Conceptual Advances in the Catalysis Science of Mixed Metal Oxide Catalytic Materials. *Catal. Today* **2005**, *100*, 79–94.

(76) Merkle, R.; Maier, J. The Significance of Defect Chemistry for the Rate of Gas–Solid Reactions: Three Examples. *Top. Catal.* **2006**, *38*, 141–145.

(77) Montini, T.; Melchionna, M.; Monai, M.; Fornasiero, P. Fundamentals and Catalytic Applications of $CeO_2$-Based Materials. *Chem. Rev.* **2016**, *116*, 5987–6041.

(78) Campbell, C. T.; Peden, C. H. F. Oxygen vacancies and catalysis on ceria surfaces. *Science* **2005**, *309*, 713–714.

(79) Esch, F.; Fabris, S.; Zhou, L.; Montini, T.; Africh, C.; Fornasiero, P.; Comelli, G.; Rosei, R. Electron Localization Determines Defect Formation on Ceria Substrates. *Science* **2005**, *309*, 752–755.

(80) Chung, C.-H.; Tu F.-Y.; Chiu, T.-A.; Wu, T.-T.; Yu, W.-Y. Critical Roles of Surface Oxygen Vacancy in Heterogeneous Catalysis over Ceria-based Materials: A Selected Review. *Chem. Lett.* **2021**, *50*, 856–865.

(81) Che, M.; Tench, A.J. Characterization and Reactivity of Mononuclear Oxygen Species on Oxide Surfaces. *Adv. Catal.* **1982**, *31*, 77–133.

(82) Li, C.; Domen, K.; Maruya, K.; Onishi, T. Dioxygen Adsorption on Well-Outgassed and Partially Reduced Cerium Oxide Studied by FT-IR. *J. Am. Chem. Soc.* **1989**, *111*, 7683–7687.

(83) Pushkarev, V. V.; Kovalchuk, V. I.; d'Itri, J. L. Probing Defect Sites on the $CeO_2$ Surface with Dioxygen. *J. Phys. Chem. B* **2004**, *108*, 5341–5348.

(84) Martínez-Arias, A.; Conesa, J. C.; Soria, J. $O_2$-probe EPR as a Method for Characterization of Surface Oxygen Vacancies in Ceria-based Catalysts. *Res. Chem. Intermed.* **2007**, *33*, 775–791.

(85) Wu, Z.; Li, M.; Howe, J.; Meyer, H. M.; Overbury, S. H. Probing Defect Sites on $CeO_2$ Nanocrystals with Well-Defined Surface Planes by Raman Spectroscopy and $O_2$ Adsorption. *Langmuir* **2010**, *26*, 16595–16606.

(86) Schilling, C.; Hofmann, A.; Hess, C.; Ganduglia-Pirovano, M. V. Raman Spectra of Polycrystalline $CeO_2$: A Density Functional Theory Study. *J. Phys. Chem. C* **2017**, *121*, 20834–20849.

(87) Etim, U. J.; Bai, P.; Gazit, O. M.; Zhong, Z. Low-Temperature Heterogeneous Oxidation Catalysis and Molecular Oxygen Activation. *Catal. Rev.* **2023**, *65*, 239–425.

(88) Guzman, J.; Carrettin, S.; Corma, A. Spectroscopic Evidence for the Supply of Reactive Oxygen During CO Oxidation Catalyzed by Gold Supported on Nanocrystalline $CeO_2$. *J. Am. Chem. Soc.* **2005**, *127*, 3286–3287.

(89) Choi, Y. M.; Abernathy, H.; Chen, H.-T.; Lin, M. C.; Liu, M. Characterization of $O_2$-$CeO_2$ interactions Using in situ Raman Spectroscopy and First-Principle Calculations. *ChemPhysChem* **2006**, *7*, 1957–1963.

(90) Camellone, M. F.; Fabris, S. Reaction Mechanisms for the CO Oxidation on $Au/CeO_2$ Catalysts: Activity of Substitutional $Au^{3+}/Au^+$ Cations and Deactivation of Supported $Au^+$ Adatoms. *J. Am. Chem. Soc.* **2009**, *131*, 10473–10483.

(91) Wang, Y.-G.; Mei, D.; Glezakou, V.-A.; Li, J.; Rousseau, R. Dynamic Formation of Single-atom Catalytic Active Sites on Ceria-supported Gold Nanoparticles. *Nat. commun.* **2015**, *6*, 6511.

(92) Soler, L.; Casanovas, A.; Escudero, C.; Perez-Dieste, V.; Aneggi, E.; Trovarelli, A.; Llorca, J. Ambient Pressure Photoemission Spectroscopy Reveals the Mechanism of Carbon Soot Oxidation in Ceria-Based Catalysts. *ChemCatChem* **2016**, *8*, 2748–2751.

(93) Schilling, C.; Ziemba, M.; Hess, C.; Ganduglia-Pirovano, M. V. Identification of Single-atom Active Sites in CO Oxidation Over Oxide-supported Au Catalysts. *J. Catal.* **2020**, *383*, 264–272.

(94) Piliai, L.; Matvija, P.; Dinhová, T. N.; Khalakhan, I.; Skála, T.; Doležal, Z.; Bezkrovnyi, O.; Kepinski, L.; Vorokhta, M.; Matolínová, I. In Situ Spectroscopy and Microscopy Insights into the CO Oxidation Mechanism on $Au/CeO_2$(111). *ACS Appl. Mater. Interfaces* **2022**, *14*, 56280–56289.

(95) Wang, J.; Cheng, D.; Chen, F.; Zhan, X. Chlorine-Decorated Ceria Nanocubes for Facilitating Low-Temperature Cyclohexane Oxidative Dehydrogenation: Unveiling the Decisive Role of Surface Species and Acid Properties. *ACS Catal.* **2022**, *12*, 4501–4516.

(96) Su, Z.; Li, X.; Si, W.; Artiglia, L.; Peng, Y.; Chen, J.; Wang, H.; Chen, D.; Li, J. Probing the Actual Role and Activity of Oxygen Vacancies in Toluene Catalytic Oxidation: Evidence from In Situ XPS/NEXAFS and DFT + U Calculation. *ACS Catal.* **2023**, *13*, 3444–3455.

(97) Zhu. Y.; Wang, J.; Patel, S.B.; Li, C.; Head, A.R.; Boscobinik, J.A.; Zhou, G. Tuning the Surface Reactivity of Oxides by Peroxide Species. *Proc. Natl. Acad. Sci. U. S. A.* **2023**, *120*, e3315189120.